

CARBON AND OXYGEN ISOTOPIC RATIOS FOR NEARBY MIRAS

KENNETH H. HINKLE

*National Optical Astronomy Observatory
P.O. Box 26732, Tucson, AZ 85726 USA*

khinkle@noao.edu

and

THOMAS LEBZELTER

*Department of Astrophysics, University of Vienna
Türkenschanzstrasse 17, 1180 Vienna, Austria*

thomas.lebzelter@univie.ac.at

and

OSCAR STRANIERO

*INAF, Osservatorio Astronomico di Collurania
I-64100 Teramo, Italy, and INFN-LNGS, Assergi (AQ), Italy*

straniero@oa-teramo.inaf.it

ABSTRACT

Carbon and oxygen isotopic ratios are reported for a sample of 46 Mira and SRa-type variable AGB stars. Vibration-rotation first and second overtone CO lines in 1.5 to 2.5 μm spectra were measured to derive isotopic ratios for $^{12}\text{C}/^{13}\text{C}$, $^{16}\text{O}/^{17}\text{O}$, and $^{16}\text{O}/^{18}\text{O}$. Comparisons with previous measurements for individual stars and with various samples of evolved stars, as available in the extant literature, are discussed. Models for solar composition AGB stars of different initial masses are used to interpret our results. We find that the majority of the M stars had main sequence masses $\leq 2 M_{\odot}$ and have not experienced sizable third dredge-up episodes. The progenitors of the four S-type stars in our sample are slightly more massive. Of the six C stars in the sample three have clear evidence relating their origin to the occurrence of the third dredge-up. Comparisons with O-rich presolar grains from AGB stars that lived before the formation of the solar system reveal variations in the interstellar medium chemical composition. The present generation of low-mass AGB stars, as represented by our sample of Long Period Variables, show a large spread of $^{16}\text{O}/^{17}\text{O}$ ratios, similar to that of group 1 presolar grains and in agreement with theoretical expectations for the composition of

mass 1.2 to 2 M_{\odot} stars after the first dredge up. On the contrary, the $^{16}\text{O}/^{18}\text{O}$ ratios of present-day Long Period Variables are definitely smaller than those of group 1 grains. This occurrence is most probably a consequence of the decrease with time of the $^{16}\text{O}/^{18}\text{O}$ ratio in the interstellar medium due to the chemical evolution of the Milky Way. One star in our sample has an O composition similar to that of group 2 presolar grains originating in an AGB star undergoing extramixing. This occurrence may indicate that the extramixing process is hampered at high metallicity or, equivalently, favored at low metallicity. Similar to O-rich grains no star in our sample shows evidence of hot bottom burning, expected for massive AGB stars.

Subject headings: stars: abundances — stars: evolution — stars: interiors — stars: variables: other — ISM: abundances

1. INTRODUCTION

Mass is returned from stars to the ISM through two primary routes, supernovae explosions of massive stars and the asymptotic giant branch (AGB) stellar wind of low- and intermediate-mass stars (Sedlmayr 1994). The percentages contributed through the various evolutionary paths depend on multiple factors including metallicity but it is clear that by early in the evolution of the universe material enriched through AGB processing is present (see review by Maio & Tescari 2015). The majority of the mass return from low-mass stars to the ISM occurs in the terminal AGB stages when large amplitude pulsation plays a critical role (Vassiliadis & Wood 1993). The composition of the AGB material ejected depends on the initial stellar composition, nuclear processing, and mixing of the stellar material over the lifetime of the star. Of special interest in tracking these processes are the isotopic ratios of the light elements carbon and oxygen. There are two stable isotopes of carbon, ^{12}C and ^{13}C , and three of oxygen, ^{16}O , ^{17}O , and ^{18}O .

The atmospheric composition of the AGB stars, in addition to being important in understanding the evolution of elemental abundances, is also important in the evolution of galaxies. Abundances originating on the AGB play a key factor in the condensation of circumstellar dust around these stars. The dust from AGB stars is in turn the origin of a large fraction of interstellar grain nuclei (Gehrz 1989). Interstellar grains from the protosolar nebula have been conserved in meteorites. These dust particles can be dissected out and the isotopic ratios of carbon and oxygen measured in the lab (Hoppe 2010). This allows a comparison of abundances from interstellar dust with abundances measured in the atmospheres of AGB stars.

The surface carbon and oxygen isotopic ratios found in AGB stars are modified by CNO cycle and He burning and mixing processes that have taken place in the stellar interior over the lifetime of the star (e.g., Dearborn 1992). In a region where an incomplete CNO cycle takes place ^{13}C and ^{17}O increase whereas ^{12}C and ^{18}O are depleted. In the heart of an H-burning zone, where the temperature is higher and the CNO cycle attains the equilibrium, ^{13}C and ^{17}O are also consumed.

On the other hand, ^{12}C is the main product of He burning through the well-known 3α reaction. ^{18}O can be produced in a region where the He burning is active through α capture on ^{14}N followed by the ^{18}F β -decay. The ashes of these fundamental nucleosynthesis processes can appear at the surface as a consequence of a deep mixing. These ‘dredge-up’ events produce substantial modification of the atmospheric abundances of carbon and oxygen isotopes.

The first dredge-up (FDU) occurs in all stars of nearly solar metallicity, independent of mass, when the star leaves the main sequence and approaches the red giant branch (RGB). The second dredge-up (SDU) takes place during the early-AGB phase but only for stars of $> 4 M_{\odot}$. In both the FDU and the SDU material previously exposed to the CNO cycle is mixed and brought to the surface. A third dredge-up (TDU) occurs during the late part of the AGB phase. Recurring thermal pulses during the AGB phase caused by He-burning runaways push the external envelope of the star outward and it expands and cools. As a result shell-H burning ceases and external convective instability penetrates into the H-exhausted core. Products of He burning are mixed to the stellar surface. As a general rule the stronger the thermal pulse the deeper the following TDU episode. Models suggest that deep TDU episodes occur in the stellar mass range $1.5 M_{\odot}$ to $3 M_{\odot}$. In any case, stars less massive than about $1.2 - 1.3 M_{\odot}$ ¹ arrive on the AGB with too small an envelope and do not experience TDU. Thermal pulses are weaker in massive AGB stars so these stars experience shallower TDUs (for a review see Iben & Renzini 1983; Straniero et al. 2006).

For the most massive AGB stars ($M > 6 M_{\odot}$) another nucleosynthesis process affects the composition, hot bottom burning (HBB). In this case, the temperature at the base of the convective envelope that is always present is large enough to activate the CNO cycle and, in the most extreme cases, the Ne-Na and the Mg-Al cycles (see e.g. Doherty et al. 2014). This coupling of nuclear burning and convective mixing causes important changes of the atmospheric abundances of light isotopes.

In addition to thermal convection other processes can be responsible for the mixing of the material modified by the internal nuclear burning. Among these processes are rotational induced (meridional) mixing, magnetic buoyancy, and thermohaline circulation (Charbonnel & Lagarde 2010; Nordhaus et al. 2008). The effective importance of these phenomena in the modification of stellar chemical patterns is highly debated (Karakas et al. 2010; Busso et al. 2010; Maiorca et al. 2012). They are generically called extra-mixing processes regardless of the true nature of the underlying physical mechanism. Nevertheless, there is clear proof of the existence of one (or more) of these phenomena. When low-mass stars ($M < 2 M_{\odot}$) climb the brightest portion of the RGB $^{12}\text{C}/^{13}\text{C}$ is substantially reduced (Gilroy 1989; Gilroy & Brown 1991; Gratton et al. 2000; Abia et al. 2012). For solar metallicity stars this reduction may be up to 50% of the value attained after the first dredge-up. Similar evidence is also found in some low-mass AGB stars (Lebzelter et al. 2008) but it does not seem a general rule (Lederer et al. 2009).

¹The limit depends on the pre-AGB mass loss and on the initial chemical composition.

Not surprisingly it also has been demonstrated that initial isotopic compositions differ between stars. In a previous article we studied the oxygen isotopic composition of a few giant stars belonging to open clusters of known age with distance from the galactic center between 8 and 10 kpc, similar to that of the sun. We found that the initial oxygen isotopic ratios of these open clusters were different from those measured in the solar system (Lebzelter et al. 2015). This presents a further complication in the interpretation of the observed isotopic abundances in terms of physical phenomena taking place during the stellar lifetime.

In this paper, we present new measurements of carbon and oxygen isotopic ratios in a large sample of long period variables (LPVs). Our sample is limited to large amplitude LPVs of the Mira and SRa variable classes clearly placing these objects on the AGB (Wood 2015). The Mira LPVs are the most luminous of the LPV family of variables and represent the fundamental mode pulsators (Wood 2015). Mass-loss rate increases exponentially with pulsation period for Miras with period below ~ 800 days (Vassiliadis & Wood 1993). At extremely long period the stars become obscured by circumstellar dust. Our sample includes only unobscured stars with period < 600 days.

Abundance measurements in LPVs can be directly compared with both theoretical expectations for AGB models and abundances measured in presolar grains. However, LPV spectra are notoriously difficult to analyze. The optical spectrum is dominated by scattering processes (Ireland et al. 2008). The photospheric lines, which can be detected only in the infrared, undergo large temperature and velocity variations (Hinkle et al. 1982). Model atmospheres and spectrum synthesis techniques are clearly limited in dealing with these spectra (McSaveney et al. 2007; Lebzelter et al. 2014). Here we employ an empirical technique that utilizes broad-band near-IR spectra and is best suited for the analysis of isotopomers. In the following section we will discuss the analysis of the spectra and then discuss the resulting isotopic ratios.

2. OBSERVATIONS AND REDUCTIONS

The observational material in this paper is drawn entirely from the archives of the Kitt Peak National Observatory (KPNO) 4-meter Mayall telescope Fourier Transform Spectrometer (FTS). All the program stars are AGB variables, restricted to those that are Mira and SRa variables. We differentiated between the various classes of SR type variables using the latest General Catalog of Variable Stars (GCVS). In a few cases we have included variables with GCVS classification of SRb but with an amplitude of an SRa. The complete set of spectra used for this project is listed in Table 1.

The FTS was operated between the years 1975 and 1995 by KPNO as a coude instrument on the Mayall Telescope (Hall et al. 1979). FTS technology provides high throughput but lacks multiplex advantage (Ridgway & Hinkle 1992) and as a result is suitable only for observations of bright objects. The redeeming features of FTS include a large number of desirable instrumental characteristics such as very large wavelength coverage, no scattered light, and well defined instru-

mental profile. Hence the wide application of this technique in laboratories but not in ground-based night-time astronomy. This said, over the lifetime of the Mayall FTS thousands of bright stars in the northern sky were observed. Many of the brightest stars in the infrared sky are variable AGB stars and a rich selection of Mira spectra were archived. Many of these are in time series.

All the program stars were observed in a broad band-pass mode covering the 1.5 to 2.5 μm spectral region. The band-pass filters employed were a green glass filter to block long wavelengths and a 1.6 μm interference long-pass filter. Both filters were wedged and the combination is free of fringing. The transmission curve is smooth and featureless except for a 10% absorption in the glass from about 2.2 to 2.3 μm . The smoothness of the filter transmission and very large wavelength coverage are useful for estimating the continuum. While the band pass and sampling characteristics of the spectra became largely uniform after the commissioning of the facility instrument in 1979, the broad spectral response depended on the beamsplitter coatings. Due to required maintenance for exposed optical surfaces the coatings were replaced several times over the lifetime of the instrument. In analyzing the data for this paper we found that optimizing these coatings for the much requested *K* band resulted in decrease in the bluest *H* band response by about a factor of two after 1982.

Rather than wavelength the natural unit of an FTS is inverse wavelength, i.e. wavenumber (σ). Following standard convention we use cm^{-1} units. The spectral sampling ($\Delta\sigma$) is constant in wavenumber and typically $\sim 0.070 \text{ cm}^{-1}$ for this data set. This corresponds to spectral resolution ($R = \sigma/\Delta\sigma$) ~ 57000 at the red end ($4000 \text{ cm}^{-1} = 2.5 \mu\text{m}$) of the spectrum and $R \sim 96000$ at the blue end ($6670 \text{ cm}^{-1} = 1.5 \mu\text{m}$). A few spectra of slightly lower resolution are used as well. The lowest resolution used in this paper is 0.15 cm^{-1} which corresponds to $R = 27000$ at the red end of the spectrum. FTS spectra are typically apodized to dampen the side lobes of the sinc function instrumental profile. Damping the amplitude of the instrumental profile side lobes lowers the resolution and results in a corresponding increase in signal-to-noise. All spectra taken after about 1979 have been apodized by function I2 of Norton & Beer (1976). Prior to 1979 a prototype FTS was employed that had path-dependent vignetting. This resulted in an instrumental apodization and we have not apodized these spectra. The choice of apodizing function is shown in the Table of Observations (Table 2).

The limiting *K*-band magnitude for the broadband observations discussed in this paper was about +1. At this limiting magnitude the observation of hot stars for use as telluric standards is very time consuming. Most of the program stars were short observations, frequently filling a short time slot in another program, and telluric reference spectra were not observed. The measurement technique depends on observing many lines and those lines blended with telluric features are easily discarded. Hence no attempt has been made to correct the spectra for telluric absorption using, for instance, telluric synthesis techniques.

Visual phases have been computed for the sample stars where data from the AAVSO were available. Wherever possible the maximum directly preceding our observation was used as a reference point. In a few cases the time of the maximum could not be determined accurately due to the

lack of sufficient data. These cases are marked with a colon in Table 2. Periods were taken from the GCVS. For stars where we found additional period determinations in the literature we determined the period at the time of the observation by measuring the time difference to the next maximum.

The spectra were taken for other projects, mainly to monitor kinematics. Many spectra have previously been discussed in the literature (Hinkle et al. 1982, 1984, 1997, 2000; Lebzelter et al. 1999). Where multiple spectra of a star exist we have, when possible, selected spectra with the best signal-to-noise and phases that are post-maximum. Work on stellar kinematics shows that the photospheric spectrum is simplest and richest a few tenths of a period after maximum. In a few cases we have analyzed multiple phases. For some stars only one spectrum is available and selection of phase is not possible.

3. ANALYSIS

3.1. Curve of Growth Analysis

The stellar sample discussed here consists entirely of large amplitude AGB variables, Miras and SRa variables. As mentioned above spectrum synthesis for these objects continues to be beyond the grasp of model atmospheres and line modeling techniques (Lebzelter et al. 2014). To undertake a first analysis of isotopic ratios in these stars we have turned to a largely empirical technique. The first and second overtone CO lines in the $2.3 - 2.5 \mu\text{m}$ and $1.5 - 1.8 \mu\text{m}$ regions, respectively, were employed. As noted above the observed spectra cover the entire $1.5 - 2.5 \mu\text{m}$ region allowing both overtones to be analyzed in a single spectrum. The basic reduction techniques have been discussed in Hinkle et al. (1976), Hinkle (1978), and Hinkle et al. (1982). A similar technique for measuring isotopic ratios can also be found in Dominy & Wallerstein (1987). These papers employ curve of growth (CoG) analysis. CoG is a classical technique for deriving elemental abundances that includes many simplifying assumptions that can be dealt with more thoroughly through spectrum synthesis. However, CoG is a powerful technique if only isotopic ratios are derived. The comparison of curves of growth for isotopically substituted molecules remove many of the uncertainties associated with the atmospheric structure. We briefly describe our approach in this section.

As a first step, the continuum was set by using high points across the entire band pass. The technique typically works well owing to a featureless filter transmission function with gentle curvature at the edges. However, Mira variables have emission lines at pre-maximum phases (Hinkle & Barnes 1979; Hinkle et al. 1982) that can result in a high continuum placement. When possible in this analysis we have not used phases when emission lines can be present, between roughly 0.8 and 0.0. For some objects we had no choice but to use spectra in this range of phases. In these cases we examined the high points at high resolution to attempt to determine if they were emission lines.

The velocity of the most abundant CO isotopologue, $^{12}\text{C}^{16}\text{O}$, was determined from the second

overtone lines using cross correlation against laboratory line positions. This velocity was used to set the apparent wavelengths of all first and second overtone CO transitions in the filter band pass. FTS spectra have an intrinsically accurate wavenumber scale and do not depend on a dispersion relation. Our technique makes use of accurate wavenumber scale. A line list was generated covering the vibration-rotation lines expected under LTE in cool (2000 – 4000 K) star atmospheres. The depths of all spectral lines at the line list positions were measured. Plots of line central depth versus rotational quantum number were produced for each vibration transition. The depths form a conspicuous lower bound with a distinctive shape (Figure 1) resulting from the rotational population (Herzberg 1950). A line list was produced from the lines at the lower bound. The equivalent widths of the lines in the list were measured and a calibration of central depth to equivalent width produced. To check on the validity of the selected lines we compared the lists for the program stars. Lists of lines for the various CO isotopologues that are in common to at least four stellar spectra are given in the appendices.

The analysis proceeds by assuming a Planckian source function and an isothermal atmosphere. The isothermal atmosphere, while a very crude assumption, reflects the excitation temperature of the molecular line forming region. With these assumptions there is a simple relation between the strength of the spectral line, the excitation energy of the line and the excitation temperature of the gas in the stellar atmosphere (Hinkle et al. 1976). By minimizing the separation in the curves of growth between high and low excitation lines a value for the excitation temperature can be established. The excitation temperature was set from the rich selection of lines in the $^{12}\text{C}^{16}\text{O}$ second overtone and applied to all the overtones and isotopes. The isotopic ratio is measured from the shift between the different curves (Figure 2).

The use of one molecule combined with comparing lines of similar strength and excitation eliminates many complications. In a typical case $^{12}\text{C}/^{13}\text{C}$ is determined from CO second overtone lines spanning a large range of vibrational transitions with ^{13}CO mid-excitation lines having the same depth as ^{12}CO low and high excitation lines. As a result the isotopic ratio will be temperature sensitive. On the other hand the ^{17}O isotope was measured using mainly the lines 2-0 C^{17}O R 25 to 33. In this case only a small range of excitation energy is probed. The line depths are typically similar to 3-0 $^{12}\text{C}^{16}\text{O}$ lines that have similar excitation energy so there is little temperature sensitivity. As part of the evaluation of the uncertainties the excitation temperature was varied through a reasonable range.

3.2. Isotopic ratios

As described in the previous paragraphs, the isotopic ratio is determined from the shift in the abscissa between the two CoG, e.g., one for ^{12}CO and one for the rarer isotope. An illustration of this method is given in Figure 2 for the Mira T Cep. The reduced equivalent width, W_σ/σ , is shown as a function of the LTE line strength, $(gf/Q(T))10^{-\Theta\chi}$, where W_σ the equivalent width in wavenumbers, σ is the wavenumber of the transition, g is the statistical weight (for

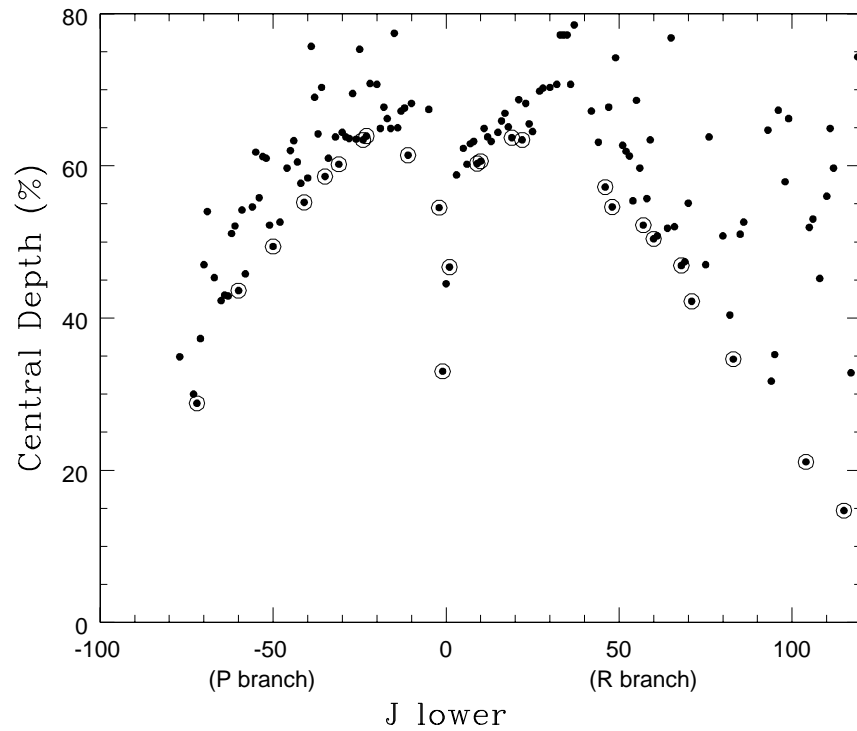


Fig. 1.— Central depth measurements for the P and R branches of the $^{12}\text{C}^{16}\text{O}$ 4-1 band in T Cep 77 Nov 8. The J' values for the P branch are shown as negative values. The circled points were selected as least blended and used in the curve of growth analysis.

vibration-rotation CO $g=2J''+1$), f is the oscillator strength, Θ is 5040 divided by the excitation temperature, χ is the energy of the lower level of the transition, and $Q(T)$ is the partition function that includes the relative number of particles of the studied species. The CO wavenumbers and excitation energies were computed from George et al. (1994). The oscillator strengths are from Goorvitch & Chackerian (1994a,b). Isotopic ratios determined for the program stars are listed in Table 2.

The CoG shown in Figure 2 is also typical in the sense that the lower left end of the CoG is less clearly defined with larger scatter resulting from a relatively larger noise contribution to the weaker lines. In some cases we see a change in the slope as the lines transition to the weak line portion of the CoG and also possibly have a larger excitation temperature. Whenever possible we tried to avoid using the weakest lines or gave these lines a lower weight. Of course in some cases isotopic lines are only represented by weak lines and this is reflected in the uncertainties.

For all stars of our sample the number of second overtone ^{12}CO lines was sufficiently large to define the CoG very well. Typically first overtone ^{12}CO lines suitable for abundance analysis are poorly represented. Only the 2-0 through 5-3 bands can be observed before the spectrum is cut off by telluric absorption near $2.5\ \mu\text{m}$. In Miras and SRa stars of near-solar abundance the first overtone ^{12}CO 2-0 lines below $J\sim 50$ are strongly saturated and lines up to $J\sim 30$ are typically blended with a line component formed in the extended atmosphere (Hinkle et al. 1982). The selection of ^{13}CO lines usually permitted a determination of the $^{12}\text{C}/^{13}\text{C}$ ratio from both the first and second overtone lines. The $^{12}\text{C}/^{13}\text{C}$ value was then determined by computing the average of both measurements. The small difference found between the two results supports the reliability of our measurements.

The $^{16}\text{O}/^{17}\text{O}$ ratios are based on at least three and typically five or more C^{17}O lines. A section of the $^{12}\text{C}^{17}\text{O}$ 2-0 band containing some of the strongest lines is well placed between other CO lines (Figure 3) and we feel the measurements of these lines are robust. For the $^{16}\text{O}/^{18}\text{O}$ ratios, the number of useable lines was smaller, and for several stars only one line was available (Figure 4). In these cases, which are marked in Table 2, the shift on the ^{12}CO CoG could not be confirmed by a second line, so that the $^{16}\text{O}/^{18}\text{O}$ ratios have to be taken with caution. The line used by Lebzelter et al. (2015), 2-0 R23, frequently appeared slightly too strong in the Mira spectra (Figure 4). The $^{16}\text{O}/^{18}\text{O}$ ratios are clearly more uncertain than the $^{12}\text{C}/^{13}\text{C}$ and $^{16}\text{O}/^{17}\text{O}$ ratios.

The isotopic ratios are found from logarithmic shifts. The uncertainty in the log is of course asymmetric in linear units. In the case of the carbon isotope ratios most authors replace the asymmetric uncertainty by a symmetric one. The absolute differences are typically small. Symmetric uncertainty was also adopted for the oxygen isotopes in this paper for the sake of consistency and easier readability. The uncertainty given is the mean between the two uncertainties, i.e., the measured uncertainty is larger in the positive direction and smaller in the negative direction than the listed value.

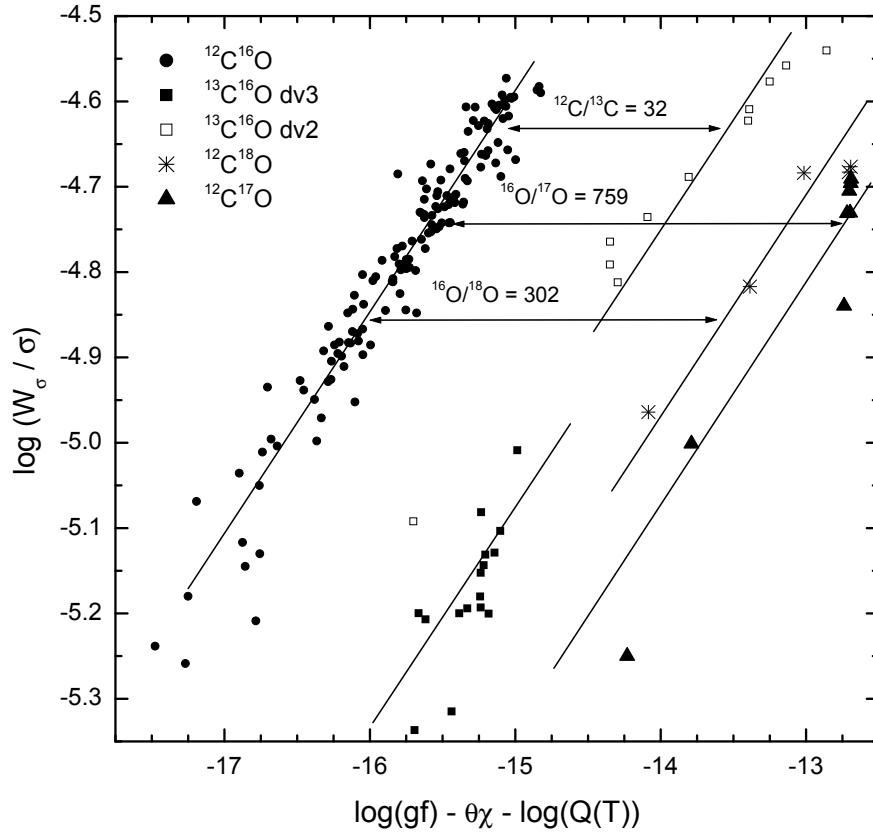


Fig. 2.— Curves of growth for near-infrared first- and second-overtone lines derived from lines of various CO isotopologues measured in the 1977 Nov 8 spectrum of T Cep. The offsets of the various curves along the x-axis are shown by arrows and the corresponding isotopic ratios are given. The excitation temperature has been set to 2900 K.

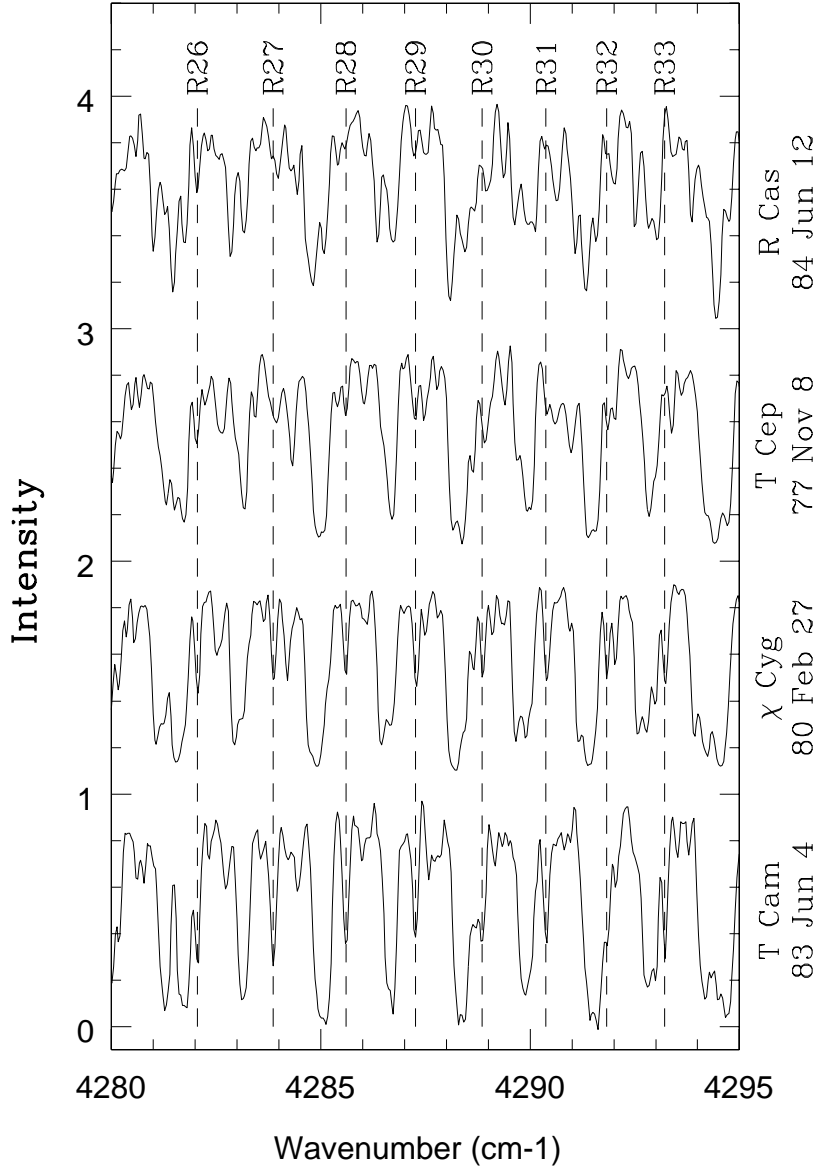


Fig. 3.— R branch $^{12}\text{C}^{17}\text{O}$ 2-0 lines identified in the spectra of four Miras. The selected Miras show a large range in $^{12}\text{C}^{17}\text{O}$ lines strengths. The spectra are shown normalized to the continuum with the $^{12}\text{C}^{17}\text{O}$ lines at the laboratory frequencies. The $^{12}\text{C}^{17}\text{O}$ 2-0 R branch lines are well placed in the spectrum and identifications are secure. The strong features are low excitation $^{12}\text{C}^{16}\text{O}$ lines.

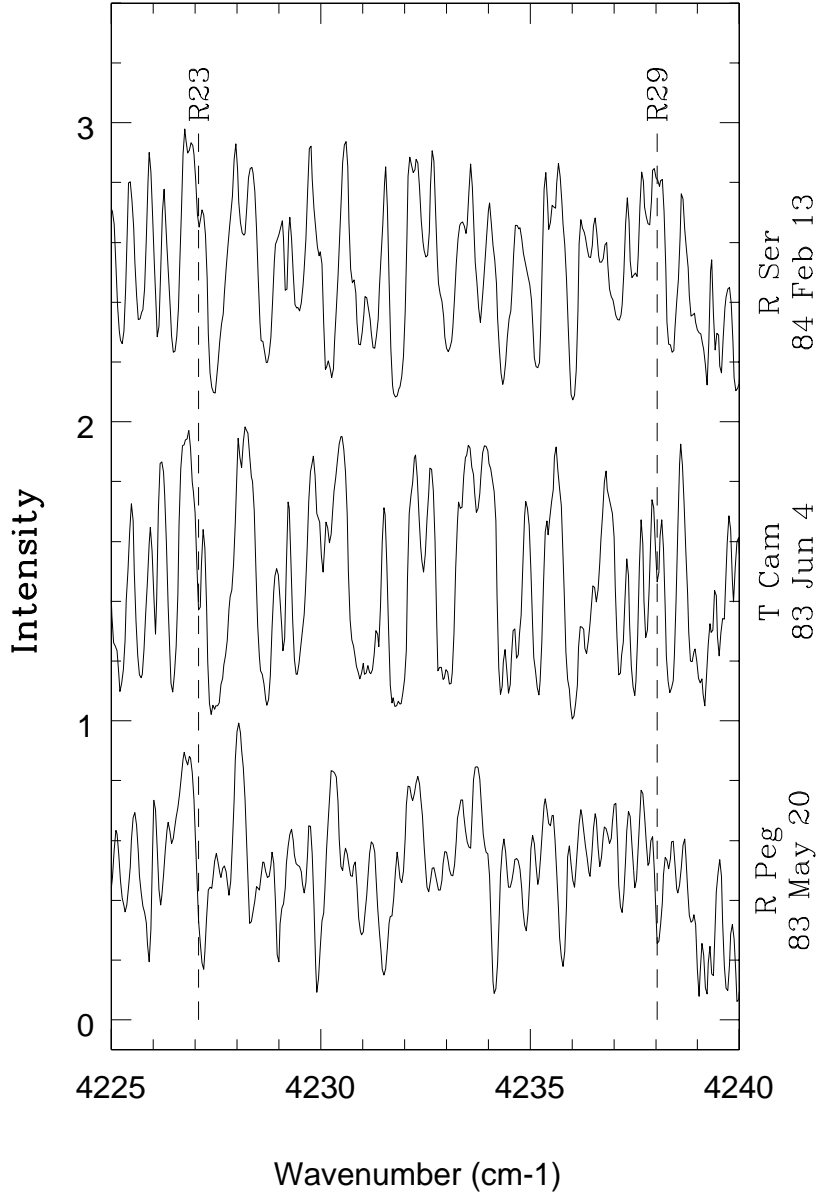


Fig. 4.— Two $^{12}\text{C}^{17}\text{O}$ 2-0 R branch lines, R23 and R29, identified in the spectra of three Miras. The selected Miras show a large range in $^{12}\text{C}^{18}\text{O}$ lines strengths. The spectra are shown normalized to the continuum with the $^{12}\text{C}^{18}\text{O}$ line at the laboratory frequencies. The $^{12}\text{C}^{18}\text{O}$ lines are poorly placed in the spectrum. The isotopic ratio generally depends on a meager selection of lines typically including either 2-0 R29 or R45. R23 which has been used by other investigators in non-variable stars, when not an obvious blend, appears slighter stronger than R29 perhaps because of an unidentified blend.

3.3. Dependence of results on pulsational phase

Third dredge up episodes in AGB stars are driven by brief helium shell flashes. While the time for these flashes can be of order a year, the resulting changes in surface luminosity (Wood & Zarro 1981) and the predicted duration of the associated dredge up are $\sim 10^2$ times longer (Pols et al. 2001). Hence we expect the surface abundances of AGB stars to be constant over time spans of a decade. Furthermore we note that none of the stars discussed in this subsection is undergoing systematic period change and so are all likely in the interpulse phase between dredge-up episodes. We take advantage of this to test the robustness of our reduction process.

Atomic and molecular spectra in LPVs are affected in a complex way by the large amplitude stellar pulsation (Lebzelter et al. 2014). The pulsation periods of these star are on the order a year. Changes of velocity and excitation temperature of the CO lines with phase are well documented. Near maximum light the lines double as a shock dissociates the molecular constituents in the atmosphere (Hinkle et al. 1984). We investigated the impact of stellar variability on our measurements of the isotopic ratios by analyzing multiple spectra in time series of observations. We selected four stars, R Cas, T Cas, o Cet and χ Cyg, with extensive time series. The $1.6 \mu\text{m}$ region of these spectra was previously analyzed by Hinkle et al. (1982) and Hinkle et al. (1984). In these two papers measurements of $^{12}\text{C}^{16}\text{O}$ and $^{13}\text{C}^{16}\text{O}$ lines were used to determine excitation temperature as a function of phase. Here we use these data to investigate the phase dependence of $^{12}\text{C}/^{13}\text{C}$.

Figure 5 shows the $^{12}\text{C}/^{13}\text{C}$ ratio versus phase for the Mira R Cas. R Cas has a near-IR spectrum with a very strong contribution from water (Hinkle et al. 2000). Water has a very rich spectrum in the $1.5\text{-}2.5 \mu\text{m}$ region with stronger lines concentrated around 1.8 and 2.5μ . The presence of blending water lines makes this star a stringent test since the selection of CO lines is not as large as in many other Miras. In fact for R Cas we could not find any clean lines for the rare oxygen isotopes. For two phases around maximum light we can derive only an upper limit on the $^{12}\text{C}/^{13}\text{C}$ ratio. In spite of this any dependence of the carbon isotopic ratio on phase is weak. We found similar results for the other stars. Spectra showing line doubling, usually appearing around maximum light in Miras, result in smaller line lists and correspondingly larger uncertainties.

The archival measurements, however, cover only the H -band. Phase dependence of the oxygen isotopes, where the lines are in the K -band, could not be studied with these data. To investigate the oxygen isotopes we measured a set of spectra of o Cet. o Cet has a spectrum that perhaps is a more difficult observational case for determining $^{12}\text{C}/^{13}\text{C}$ than R Cas. The second overtone $^{13}\text{C}^{16}\text{O}$ lines are fairly weak and, similar to R Cas, the CO spectrum is blended with a large number of water vapor lines. In Figure 6 the carbon and oxygen isotopes are shown as a function of phase. Clearly phases near maximum light give divergent values. The stronger first overtone $^{13}\text{C}^{16}\text{O}$ lines are also less reliable near maximum light due to line doubling. Overall the oxygen isotopic ratios have more scatter between measurements than is the case for the carbon isotope. This is not surprising since the line list for the oxygen isotopes is at least an order of magnitude smaller than the line list for the second overtone ^{13}CO lines.

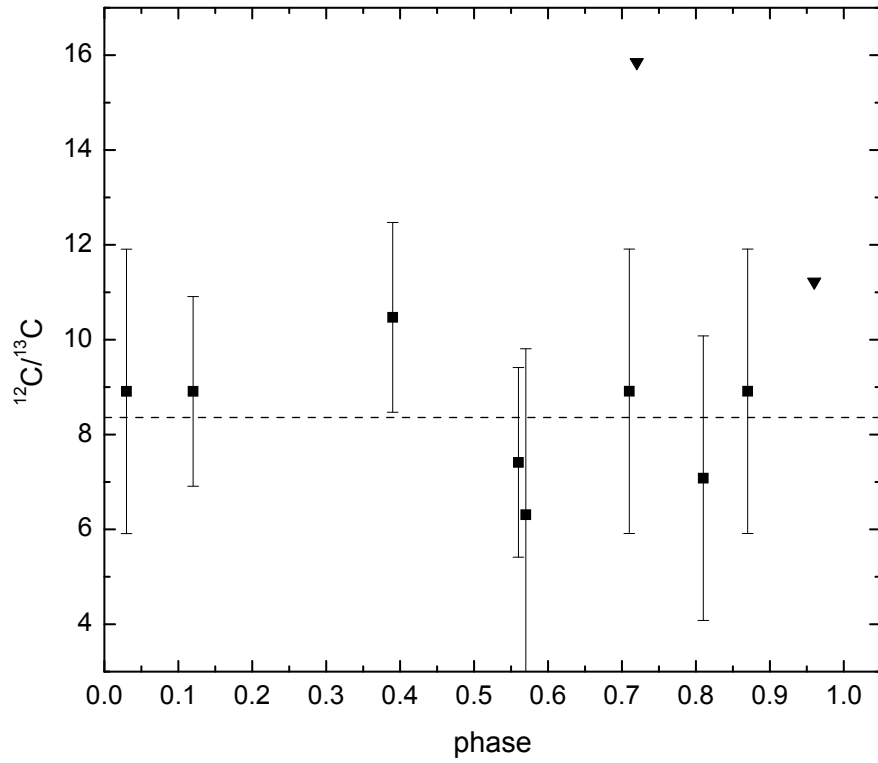


Fig. 5.— $^{12}\text{C}/^{13}\text{C}$ and associated uncertainties plotted against the phase of the measurement for the M-type Mira R Cas. For two phases (triangles) only an upper limit of the ratio could be determined. Dashed line is the mean value.

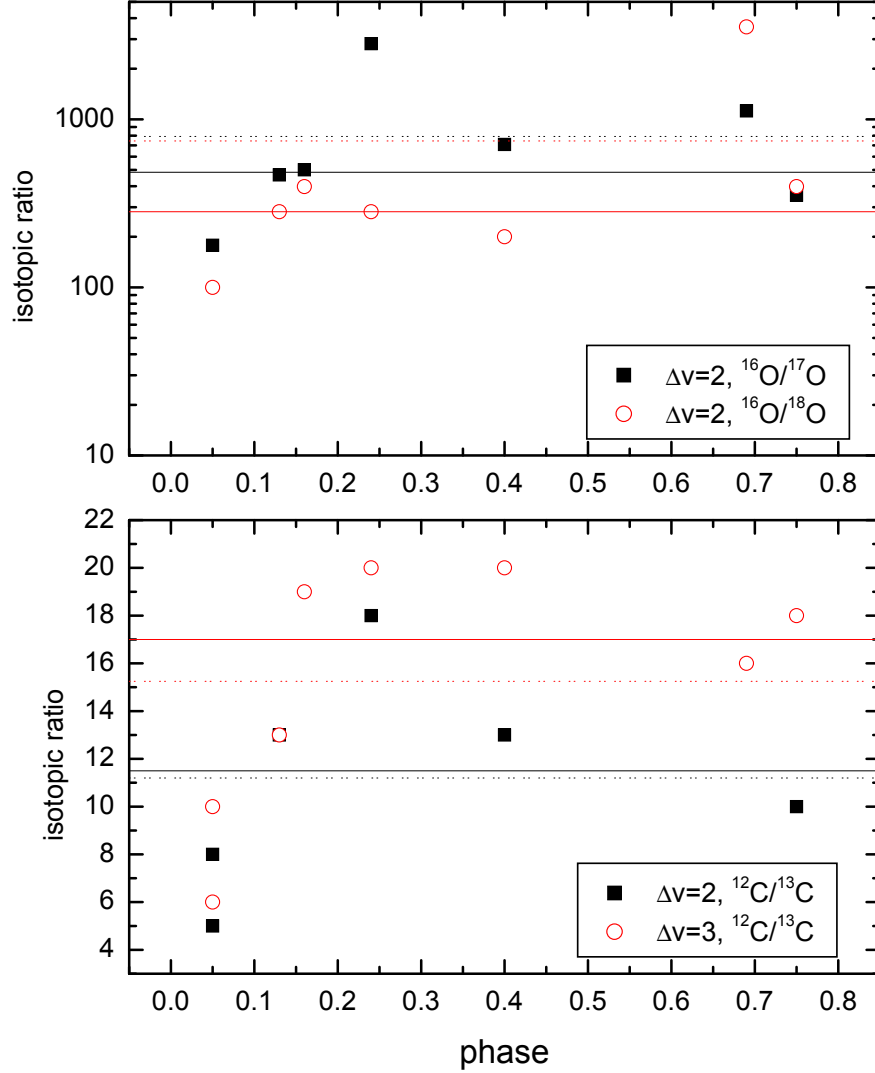


Fig. 6.— Upper panel: Oxygen isotope measurements for o Cet as a function of phase. Heavy solid line is median value for ${}^{16}\text{O}/{}^{17}\text{O}$. Light solid line is median value for ${}^{16}\text{O}/{}^{18}\text{O}$. Dotted lines are the means. Lower panel: Carbon isotopic ratios from the first and second overtone lines as as function of phase. Solid and dotted lines are medians and means.

For most stars with multiple observations in our sample the deviation from the mean value does not exceed $\pm 38\%$. For a few stars like U Ori or X Oph the difference is larger. For Table 2 we used the mean value in case of multiple observations. Note that we combine measurements from various pulsation cycles in our analysis, so that variability effects can be the result of either inter- or intra-cycle variations.

3.4. Uncertainties

The uncertainties given in Table 2 result primarily from the width of the CoG due to the scatter in equivalent widths. In the case of multiple observations, the differences between the results for each observation are also included in the uncertainty. The scatter in the CoG equivalent widths can be attributed to noise, unidentified line blends, and continuum placement. Continuum placement contributes scatter since the lines span a significant wavelength range with lines of different strengths intermingled. The equivalent widths are determined from a fit to the depths versus width relation which minimizes the effect of blending in the line widths. For the ^{13}C isotope, with a rich selection of lines, blends are likely a minor problem in the analysis. Of course, the opposite is true for the ^{18}O isotope where the result depends on only a few lines or even a single line. This effect is very difficult to quantify and may lead to significantly different isotopic ratios in individual stars. Another possible source of uncertainty is the excitation temperature used. Tests varying the excitation temperature by $\pm 200\text{ K}$ result in changes in the isotopic ratio of about 10% . Larger deviations are unlikely since this typically leads to obvious distortions in the CoG. Comparisons of these results and results obtained from spectra at different phases and consequently different excitation temperatures indicate that the uncertainties given in Table 2 are reasonable statistical estimates.

3.5. Comparison with literature data

Isotopic ratios were previously determined for a subset of our sample. In Table 3 we compare these literature values with our findings. In a few cases more than one $^{12}\text{C}/^{13}\text{C}$ value can be found in the literature. Agreement between literature values is occasionally poor, especially for three of the carbon stars, R Lep UX Dra, and V Hya. For the few cases where we found more than one oxygen isotopic ratio in the literature, we again found a range of values.

Our carbon isotopic ratios are generally in reasonable agreement with the literature values (Figure 7). A notable exception is V Hya where we derived ratio of 200 ± 50 . This is much larger than the value of 69 found by Lambert et al. (1986), 71 found by Milam et al. (2009), and 33 found by Jura et al. (1988). Agreement with the literature is clearly worse for the oxygen isotopic ratios. However, many fewer values appear in the literature. While there are a few stars where we derived very different values several measurements agree within the uncertainties. An example is the star

WHya, where Khouri et al. (2014b) derive almost identical values to our values using completely different lines.

As a final test we carried out the entire analysis on four M giants that were not LPVs. The stars selected have established values for the carbon and oxygen isotopes and were observed with the same experimental setup as the LPVs. The observations are listed at the bottom of Table 1. The results are given at the bottom of Table 3. For the M giants there is excellent agreement with the literature.

4. STELLAR EVOLUTION AND NUCLEOSYNTHESIS OF C AND O ISOTOPES

From the evolution of surface abundances, AGB stars can be roughly divided into three groups²:

- Main sequence mass $< 1.5 M_{\odot}$. These stars do not retain sufficient envelope mass to experience TDU events during the AGB phase. Their AGB surface composition is largely determined by the first dredge-up and, eventually, by the RGB extra-mixing.
- Main sequence mass between $1.5 M_{\odot}$ and $3 M_{\odot}$. These stars undergo repeated strong TDU episodes that bring to the surface the products of the He burning. The number of TDU episodes and the amount of material dredged-up depend on the efficiency of mass loss before and during the AGB phase. They are among the most important nucleosynthesis sites in all galaxies.
- Main sequence mass $> 3 M_{\odot}$. These stars undergo a second dredge-up, shallow TDU episodes, and, possibly, HBB.

The ‘super-AGB stars’ belong to the last group with main sequence masses between $8 M_{\odot}$ and $10 M_{\odot}$. After the core He burning these stars ignite carbon in a highly degenerate core and at the end of the carbon burning experience an AGB phase whose characteristics are similar to, but more extreme than, those of the AGBs with $M \sim 6 - 7 M_{\odot}$. In particular super-AGB stars are expected to experience deep HBB with temperature at the bottom of the convective envelope exceeding 10^8 K (see Doherty et al. 2010, and references therein).

In this section we summarize the results of extant nucleosynthesis calculations. Differences exist among the various models available in the literature (e.g., Lugaro et al. 2003). These stem from different choices for initial composition, numerical recipes, and values for parameters such

² The mass bounds of the three groups depend on many parameters such as initial composition and efficiency of mass loss both before and during the AGB phase. The values discussed here, representative of solar metallicity stars, are presented for guidance purposes.

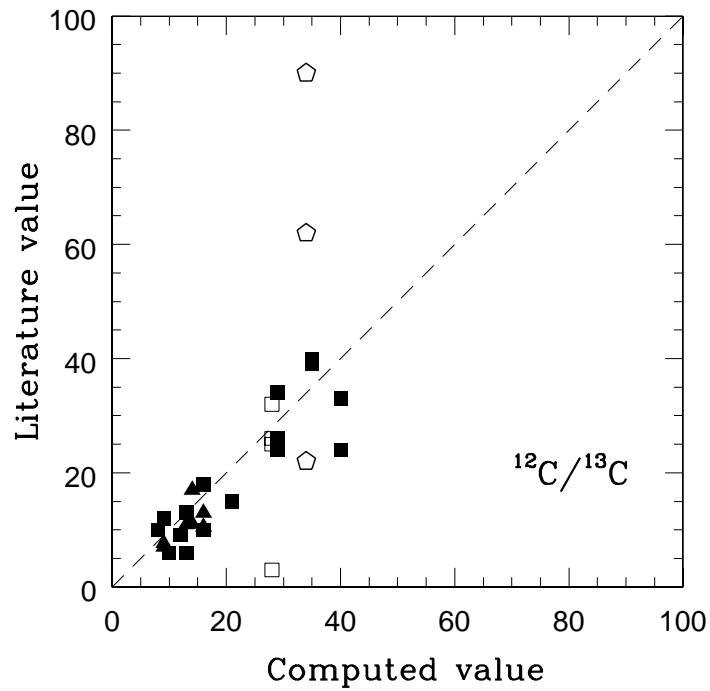


Fig. 7.— $^{12}\text{C}/^{13}\text{C}$ values computed in this paper are compared to literature values. Non-variable stars are filled triangles. The two stars with large disagreements in the literature, UX Dra and R Lep, are shown with open squares and open pentagons, respectively.

as nuclear reaction rates (for more details see section 2 in Straniero et al. 2014). Despite these differences the overall scenario is quite well established. In the following we report numerical values of the various isotopic ratios as derived from the FRUITY database (Cristallo et al. 2015, <http://fruity.oa-teramo.inaf.it/>). In general we will discuss results of models whose initial composition is solar.

4.1. Carbon isotopes

The CNO cycle depletes the most abundant carbon isotope, ^{12}C , and enhances ^{13}C . In the opposite sense, He burning is the main producer of ^{12}C . During stellar evolution the ashes of these fundamental nuclear processes are mixed with the pristine material in the stellar envelope. Mixing processes of this type, also called dredge-up episodes, are well known phenomena taking place in giant stars. Extra-mixing processes induce further modifications of the surface composition.

The carbon isotopic ratio of the sun is about 90 with galactic main sequence stars expected to share similar values. As a star leaves the MS the first dredge-up causes a reduction of the carbon isotopic ratio down to $\sim 20 - 25$. In stars with mass $< 2 M_{\odot}$ further reduction of the $^{12}\text{C}/^{13}\text{C}$ by up to a factor of two can occur as the result of RGB extra-mixing. The origin of RGB extra-mixing is unclear but its existence is confirmed by observational evidence (for a review, see Charbonnel et al. 1999). During the early-AGB phase stars with mass $\geq 4 M_{\odot}$ experience a second dredge-up. Shell H-burning temporarily ceases and external convection penetrates into the H-exhausted core. In this case, both carbon isotopes are slightly depleted so that their ratio remains almost unaltered. Therefore, $^{12}\text{C}/^{13}\text{C}$ ratios between 10 and 25 are expected at the onset of the first thermal pulse in AGB stars with different masses. The lower values, $10 < ^{12}\text{C}/^{13}\text{C} < 20$, are expected for stars with main sequence mass $< 2 M_{\odot}$. The slightly higher values, $20 < ^{12}\text{C}/^{13}\text{C} < 25$, are expected for the more massive stars. For stars undergoing recurring third dredge-up episodes the carbon isotopic ratio increases as fresh ^{12}C synthesized in the He-burning shell is mixed to the surface. The continued addition of carbon to the stellar surface layers can turn an M-type into a C-type star.

Although all AGB stars are expected to experience thermal pulses only a few are followed by third dredge-up episodes. As discussed in Straniero et al. (2003) the occurrence of TDU and its efficiency in bringing the ashes of the internal nucleosynthesis to the stellar surface depends on the core mass (M_H) and the envelope mass (M_E). The third dredge-up is inefficient in AGB stars with $M_E < 0.5$ or $M_H > 0.9 M_{\odot}$. The first condition implies the existence of a minimum stellar mass for the occurrence of the TDU. The precise value of this threshold depends on the mass lost before the beginning of the thermal pulse phase. For solar metallicity the limiting value of the main sequence mass should be $\sim 1.3 - 1.4 M_{\odot}$. Marginal TDU episodes are also seen in models of massive AGB stars that develop quite large core masses (this issue has been extensively discussed in Straniero et al. 2014). As a consequence AGB stars whose initial mass is $\lesssim 1.5 M_{\odot}$

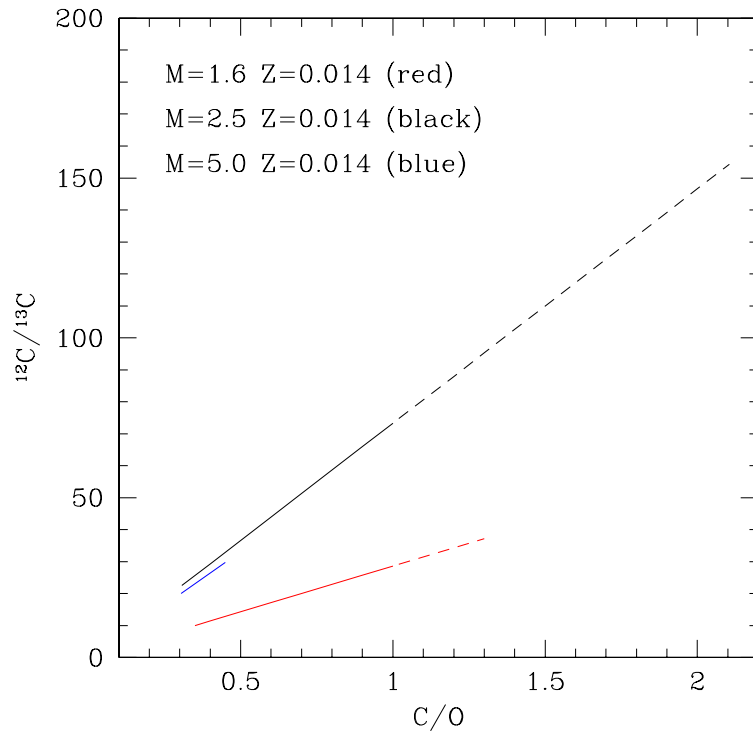


Fig. 8.— $^{12}\text{C}/^{13}\text{C}$ versus C/O for three AGB stellar models of different mass.

and $\gtrsim 5 M_{\odot}$ should appear as M stars³. Rather deep dredge-up episodes are experienced by stars with masses between 1.5 and 3 M_{\odot} so these stars may evolve into S and, possibly, C stars. The mass-loss rate determines the AGB lifetime and, hence, the maximum number of TDU episodes plays a fundamental role in the evolution to M-S-C spectral type.

The maximum $^{12}\text{C}/^{13}\text{C}$ attained by this class of AGB stars also depends on the composition at the beginning of the AGB. Figure 8 illustrates three example AGB models of initial mass 1.6, 2.5, and 5 M_{\odot} . O-rich and C-rich phases are plotted as solid and dashed lines, respectively. In the 1.6 M_{\odot} model (red line) the star arrives on the AGB with $^{12}\text{C}/^{13}\text{C}=10$ and $\text{C}/\text{O}=0.35$. These values are determined by the first dredge-up followed by RGB extra-mixing. No RGB extra-mixing has been considered in the 2.5 M_{\odot} and 5 M_{\odot} models. For these models $^{12}\text{C}/^{13}\text{C}$ is ~ 21 and $\text{C}/\text{O}\sim 0.31$ at the beginning of the AGB. Both ratios then increase because of the TDU. The final values attained at the AGB tip are $^{12}\text{C}/^{13}\text{C}=37$ and $\text{C}/\text{O}=1.3$ for $M=1.6 M_{\odot}$, $^{12}\text{C}/^{13}\text{C}=154$ and $\text{C}/\text{O}=2.1$ for $M=2.5 M_{\odot}$, and $^{12}\text{C}/^{13}\text{C}=30$ and $\text{C}/\text{O}=0.45$ for $M=5 M_{\odot}$. The two less massive models become carbon stars, i.e., attain $\text{C}/\text{O}=1$, when $^{12}\text{C}/^{13}\text{C}$ is 28 (1.6 M_{\odot}) and 71 (2.5 M_{\odot}).

In practice intrinsic C-stars, i.e., those C-stars whose origin is a direct consequence of the ongoing third dredge-up, should have carbon isotopic ratios > 25 . Lower value carbon isotopic ratios in C-stars have at least two explanations. One scenario is that an extrinsic process, for instance mass exchange or merger, caused $\text{C}/\text{O} > 1$. J-type carbon stars are likely extrinsic C-stars (Abia & Isern 1997; Abia et al. 2003). The second scenario is that the low $^{12}\text{C}/^{13}\text{C}$ ratio is a consequence of an extra-mixing process taking place during the AGB (see Abia et al. 2001; Lebzelter et al. 2008). Intrinsic S-stars, where C/O is very near but perhaps not quite 1, should have $^{12}\text{C}/^{13}\text{C} < 70$. O-rich stars with initial mass $< 1.5 M_{\odot}$ should have $^{12}\text{C}/^{13}\text{C} \sim 10 - 15$, as determined by the combined effects of the first dredge-up and the RGB extra-mixing. Slightly larger values, i.e., $^{12}\text{C}/^{13}\text{C} \sim 25 - 35$, are found for masses between 4 M_{\odot} and 6 M_{\odot} . However, if the initial mass is $> 6 M_{\odot}$, then the temperature at the base of the convective envelope may become large enough to activate the HBB. As a consequence, the $^{12}\text{C}/^{13}\text{C}$ ratio decreases. Extreme cases are found in models of super-AGB stars ($M = 8 - 10 M_{\odot}$) undergoing a very efficient HBB. They show $^{12}\text{C}/^{13}\text{C}$ as low as 3 – 5, the typical equilibrium value of the CN cycle (e.g., Doherty et al. 2014).

4.2. Oxygen isotopes

^{18}O is depleted by H burning whereas ^{17}O is enhanced. ^{16}O is depleted but at a rather high temperature. On the contrary, both ^{16}O and ^{18}O are produced by He burning through the $^{12}\text{C}(\alpha, \gamma)^{16}\text{O}$ and $^{14}\text{N}(\alpha, \gamma)^{18}\text{F}(\beta)^{18}\text{O}$ reactions. Solar values of the oxygen isotopic ratios are

³A more rapid increase of the C/O ratio is expected at low metallicity, even in AGB stars undergoing a few shallow TDU episodes. In the more massive AGBs, however, the HBB prevents the development of high C/O ratios.

$^{16}\text{O}/^{17}\text{O}= 2700$ and $^{16}\text{O}/^{18}\text{O}= 490$ (Lodders et al. 2009). In a previous paper (Lebzelter et al. 2015) we discussed theoretical predictions and uncertainties for the oxygen isotopic ratios expected after the occurrence of first dredge-up. Both oxygen isotopic ratios are sensitive to the initial composition. At variance with the $^{12}\text{C}/^{13}\text{C}$, the RGB extra-mixing has negligible effects on the oxygen isotopic ratios (see Abia et al. 2012). The reason is illustrated in Figure 9, in which we plot the variation of the C and O isotopic ratios in a typical H-burning region, i.e., the innermost layer of the H-rich envelope of a $2 M_{\odot}$ RGB model. From this plot it can be seen that extra-mixing deep enough to modify the abundances of the oxygen isotopes would imply $^{12}\text{C}/^{13}\text{C} < 5$. Note that where the $^{12}\text{C}/^{13}\text{C}$ is reduced to ~ 10 the oxygen isotopic ratios are not changed by the CNO cycle.

Assuming a solar composition the variation of oxygen isotopes with mass after the first dredge-up can be summarize as follows. $^{16}\text{O}/^{17}\text{O}$ is reduced down to a minimum value of ~ 200 in stars with $M \sim 2.5 M_{\odot}$. For smaller stellar masses the $^{16}\text{O}/^{17}\text{O}$ is larger. For instance we find $^{16}\text{O}/^{17}\text{O} = 1000$ and 2650 for models of $1.5 M_{\odot}$ and $1 M_{\odot}$, respectively. For $M > 2.5 M_{\odot}$ the $^{16}\text{O}/^{17}\text{O}$ ratio slightly increases with mass. We find $^{16}\text{O}/^{17}\text{O} = 340$ and 430 for models of 4 and $6 M_{\odot}$, respectively. The variation of ^{18}O with mass is different from ^{17}O with $^{16}\text{O}/^{18}\text{O}$ increasing after the first dredge-up because of ^{18}O consumption taking place in the H-burning zone. Values of about 700 are found for $M \geq 2 M_{\odot}$ and between 500 and 700 for smaller stellar masses.

The second dredge-up produces smaller modifications of the oxygen isotopes than the first dredge-up. In a $6 M_{\odot}$ model, we found 405 and 720 for $^{16}\text{O}/^{17}\text{O}$ and $^{16}\text{O}/^{18}\text{O}$, respectively, with 430 and 700 after the first dredge-up. Similarly, the third dredge-up does not substantially modify the abundances of the oxygen isotopes (Cristallo et al. 2015) unless a substantial overshoot at the base of the convective zone, powered by a thermal pulse, allows deep mixing of primary ^{16}O . If this is the case then both the oxygen isotopic ratios should increase at the stellar surface. However, the consequences of this overshoot on the bulk of the s-process nucleosynthesis would be dramatic (Lugaro et al. 2003). Indeed, even in low mass stars, the maximum temperature attained at the bottom of the convective zone would be large enough to activate the $^{22}\text{Ne}(\alpha, n)^{25}\text{Mg}$ reaction. The resulting high neutron density generated by this neutron source would imply a substantial modification of the s-process path at the main branching points. Large amounts of Rb and rare isotopes, like ^{96}Zr , would be synthesized which is not supported by abundance analysis of AGB stars and presolar grains (Lambert et al. 1995; Abia et al. 2001).

HBB might affect the oxygen isotopes in the more massive AGB stars. The most important effect is a significant depletion of the ^{18}O . As a result $^{16}\text{O}/^{18}\text{O}$ could became as large as 10^6 (Boothroyd et al. 1995). In the most extreme cases ^{16}O and ^{17}O could also decrease. It should be recalled, however, that a quantitative analysis of HBB is still hampered by many uncertainties. Briefly, the nuclear burning timescales of the various isotopes involved in the nucleosynthesis processes vary over several orders of magnitude. Some of these timescales are smaller, some are comparable to, and some definitely larger than the mixing timescale, i.e., the time required to move a nucleus from the bottom to the top of the convective envelope. As a consequence the results of

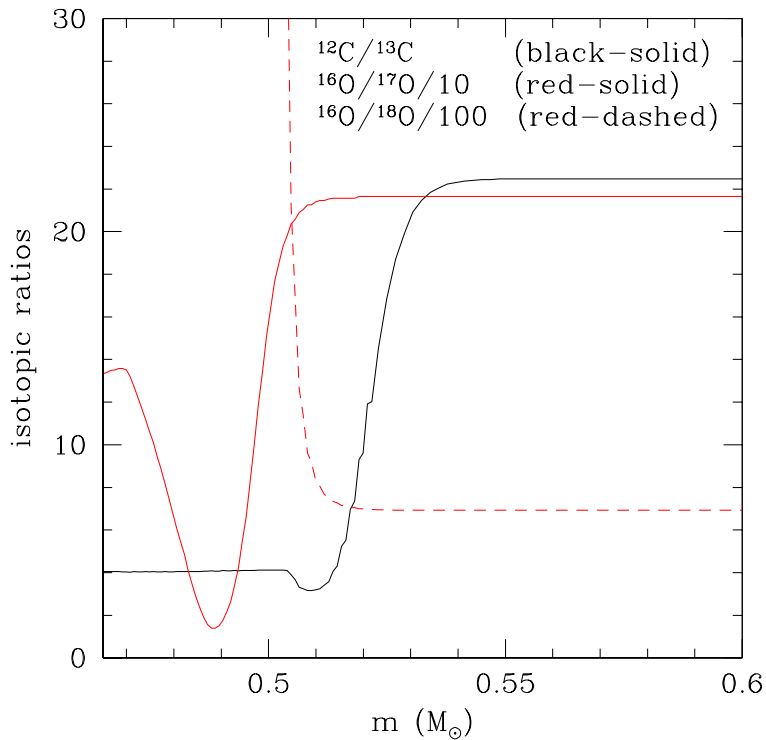


Fig. 9.— Carbon and oxygen isotopic ratios in the innermost layer of the H-rich envelope of a $2 M_{\odot}$ RGB model. The variation of the $^{12}\text{C}/^{13}\text{C}$ starts in a relatively external region where the temperature is $T > 10$ MK. The variations of the oxygen isotopes take place more internally where $T > 15$ MK.

the nucleosynthesis calculations are sensitive to the details of the adopted mixing algorithm, in particular to those related to the coupling of mixing and burning.

Summarizing, with the exception of the more massive AGB and super-AGB stars undergoing HBB the oxygen isotopic ratios in LPVs should coincide with those left by the first dredge-up. No significant differences are expected among M, S, and C stars having similar mass. The majority of the intrinsic S and C stars, typically having masses ranging between 1.5 and 3 M_{\odot} , should have $^{16}\text{O}/^{17}\text{O}$ roughly confined between 200 and 1000. M stars, which can be less massive, can show larger $^{16}\text{O}/^{17}\text{O}$ ratios up to about 2700 (see also models by Karakas et al. 2010). On top of the variations of these ratios with stellar mass a spread of the observed values is likely due to a spread of the initial abundances of the oxygen isotopes.

The theoretical scenario described so far is summarized in Figure 10. As a consequence of a deep mixing process the $^{12}\text{C}/^{13}\text{C}$ usually decreases except in the case of the third dredge-up. $^{16}\text{O}/^{17}\text{O}$ can only decrease but $^{16}\text{O}/^{18}\text{O}$ always increases. Therefore $^{16}\text{O}/^{18}\text{O}$ ratios smaller than the solar value, like those observed in open cluster giants (Lebzelter et al. 2015), necessarily indicate a variation of the oxygen isotopic composition with respect to the solar, in particular ^{18}O enhanced and/or ^{16}O depleted. Moreover, the $^{16}\text{O}/^{17}\text{O}$ ratio is a good tracer of the stellar mass.

5. DISCUSSION

5.1. Carbon isotopes

The $^{12}\text{C}/^{13}\text{C}$ ratio is often used as an indicator of mixing processes in evolved stars. It is measurable using a number of different observational approaches. $^{12}\text{C}/^{13}\text{C}$ is typically smaller than the oxygen isotopic ratios and hence more easily determined. Large sets of values, primarily for non- or only slightly variable evolved stars, are available in the literature. In Figure 11 we compare the distribution of the $^{12}\text{C}/^{13}\text{C}$ for our sample with $^{12}\text{C}/^{13}\text{C}$ distributions for giants, AGB stars and carbon stars in published data sets.

The samples compared in Figure 11 cover very different groups of evolved stars. Our data are dominated by large amplitude LPVs with most stars of M-type. Four of our sample stars are classified as spectral type S, six as spectral type C, and just one as type SC. The Mira SCep has a $^{12}\text{C}/^{13}\text{C}$ ratio too large to be shown on this plot. The peak in our distribution (top panel of Figure 11) is for $^{12}\text{C}/^{13}\text{C}$ between 10 and 20. This indicates a sample biased toward low-mass stars. This is in contrast to the second sample plotted in Figure 11 which is from Gilroy (1989) and consists of late-type giants in open clusters. The Gilroy (1989) distribution peaks between 20 and 30. Indeed, the stars in the Gilroy (1989) sample are progenitors of AGB stars with masses between 1.6 and 6 M_{\odot} . Another sample of likely AGB progenitors is the one by Tomkin et al. (1976) consisting of late-type field giants. This sample likely includes a mixture of low- and intermediate-mass stars. In agreement with this assumption the $^{12}\text{C}/^{13}\text{C}$ values concentrate between 10 and

30.

The sample of Ramstedt & Olofsson (2014) is dominated by AGB stars. Indeed there are several stars in common between the Ramstedt & Olofsson (2014) sample and our sample (see Table 3). However, unlike our sample the Ramstedt & Olofsson (2014) sample has M-, S-, and C-type stars roughly equally represented. The histogram (fourth panel from the top in Figure 11) peaks between 10 and 20 like our data. Interestingly, a larger fraction of stars with $^{12}\text{C}/^{13}\text{C} < 10$ are present in the Ramstedt & Olofsson (2014) sample than in our sample. At the same time, the fraction of stars with $^{12}\text{C}/^{13}\text{C} > 20$ is lower. It is worth noting that the study of Ramstedt & Olofsson (2014) is the only one in our comparison that is based on radio data while all the other authors used optical and/or infrared spectra for their analysis. The use of radio data implies that the stars are undergoing significant mass loss.

The final two literature samples shown in Figure 11 consist of C stars only. Both samples show similar histograms with two peaks, one at very low $^{12}\text{C}/^{13}\text{C}$ ratios and one above 40. There are a few C-stars with $^{12}\text{C}/^{13}\text{C} > 80$ which are not plotted for the sake of clarity. The sample of Abia & Isern (2000) consists of J-type carbon stars with $^{12}\text{C}/^{13}\text{C}$, by definition, lower than 15. Nevertheless, in the sample of Abia et al. (2001) there are C stars classified as N-type with $^{12}\text{C}/^{13}\text{C} < 25$. Such an occurrence is considered a proof of the occurrence of AGB extramixing.

5.2. Oxygen isotopes

In addition to $^{12}\text{C}/^{13}\text{C}$, $^{16}\text{O}/^{17}\text{O}$ is also a good stellar mass tracer. The upper panel of Figure 12 shows the areas in the $^{12}\text{C}/^{13}\text{C}$ versus $^{16}\text{O}/^{17}\text{O}$ diagram occupied by AGB stars of different masses. Values for stars included in our sample are shown in the lower panel. Our sample stars cover the same range in this parameter space expected for AGB stars with masses below $3 M_{\odot}$. The selection of our sample was driven primarily by apparent near-infrared brightness and variability. The sample reflects a mass range typical for Miras in the solar neighborhood. The number of objects with $^{16}\text{O}/^{17}\text{O}$ below 1000 is clearly larger than those with higher $^{16}\text{O}/^{17}\text{O}$ indicating that the majority of the Miras have main sequence masses $\sim 1.5 M_{\odot}$. The typical mass range is then around 1.5 to $2 M_{\odot}$ for most Miras with a smaller fraction having masses of less than $1.5 M_{\odot}$.

$^{16}\text{O}/^{18}\text{O}$, on the other hand, is almost insensitive to initial mass but can be a good tracer of the oxygen composition either in the gas from which the stars were formed and/or from particularly deep mixing processes like the HBB. The distribution of our sample stars in the $^{16}\text{O}/^{18}\text{O}$ versus $^{16}\text{O}/^{17}\text{O}$ diagram is shown in Figure 13. Model predictions for AGB stars with solar composition and enhanced original ^{18}O abundance are shown. While we have to keep in mind that our $^{16}\text{O}/^{18}\text{O}$ measurements have higher uncertainties than the $^{16}\text{O}/^{17}\text{O}$ and $^{12}\text{C}/^{13}\text{C}$ measurements, the diagram suggests that there exists a range of initial $^{16}\text{O}/^{18}\text{O}$ values in the sample stars. Either a reduced initial ^{16}O abundance or an enhanced initial ^{18}O abundance compared to the solar value is required for the majority of the stars. M-, S-, and C-type stars do not differ in this respect. The predicted

dependency on mass may be weakly visible in our observations but the measurement uncertainties are simply too large to reach a clear conclusion.

5.3. M stars

Spectral type M AGB stars are not polluted with third dredge-up material. Typically these stars have a mass too low to experience third dredge-up events. However, it is possible that the M AGB stars include stars of higher mass at the beginning of AGB evolution, i.e., before experiencing a significant change of surface composition by third dredge-up. The spectral type alone is insufficient to further constrain the mass of a particular LPV. The isotopic ratios permit additional conclusions. Once the star has experienced several third dredge-up events, changes in the abundance of s-process elements permit constraints on mass. In the case of a massive AGB star experiencing HBB the C/O and the $^{12}\text{C}/^{13}\text{C}$ can be maintained at low levels in spite of the TDU but some s-process enhancement will occur. It is possible that the HBB prevents or, at least, makes the TDU very weak (Straniero et al. 2014). These objects will be very rare compared to the less massive AGB.

The majority of the M-type stars in our sample have $^{12}\text{C}/^{13}\text{C}$ between 10 and 20. They have not experience third dredge-up but most probably have experienced some extra-mixing on the RGB. Their mass should be smaller than $\sim 2 M_{\odot}$. A part of this sample shows $^{16}\text{O}/^{17}\text{O} > 1000$ limiting their mass further to below $1.5 M_{\odot}$ (see Figure 12). About two thirds of the M-type stars with $^{12}\text{C}/^{13}\text{C} < 20$ show $^{16}\text{O}/^{17}\text{O}$ values more compatible with a mass above $1.5 M_{\odot}$ (lower left corner of Figure 12). The masses of this set can thus be constrained quite well to a range between 1.5 and $2 M_{\odot}$. This is consistent with other mass estimates for Miras in the same period range recently summarized by Feast (2009).

Our sample is entirely made up of Mira and SRa variables. These are fundamental mode AGB pulsators associated with the final stage of the AGB evolution (see Wood 2015, and references therein). This suggests that our sample stars are not at the beginning of the AGB phase. We expect a slow increase of the surface carbon isotopic ratio as stars evolve along the AGB. Since we measure $^{12}\text{C}/^{13}\text{C}$ below 20 we see four possibilities to interpret this finding. While we feel options become increasing unlikely with position on the list we can not exclude any of them on the basis of observations.

1. The carbon isotopic ratio was very low in these stars on their arrival on the early AGB. Carbon isotopic ratios as low as 10 – 15 are observed for low mass RGB stars of near-solar metallicity (Charbonnel et al. 1998). Should the star experience thermal pulses without or with only minor third dredge-up mixing (e.g., Lebzelter & Hron 2003) a ratio between 10 and 20 is compatible with theory.
2. Extra-mixing may occur on the AGB (Karakas et al. 2010; Busso et al. 2010). Lebzelter et al. (2008) brought up this process in order to interpret the unexpectedly low $^{12}\text{C}/^{13}\text{C}$ ratios observed in C-stars in the LMC cluster NGC 1846. The AGB stars in this cluster are thought to be of similar

mass, i.e., around $1.5 M_{\odot}$, to the field Miras but with different metallicity.

3. Variability studies demonstrating that Mira variability is limited to the final AGB stages are only for the Magellanic Clouds and globular clusters (see for instance Wood 2015). Magellanic Clouds and globular clusters stars typically have sub-solar metallicity. Until the Gaia results are compiled the luminosities of Galactic field Miras remain poorly known. It is possible that at higher metallicity Mira variability is not limited to stars near the termination of the AGB.

4. Some of the sample stars could be massive AGBs in which the HBB regulates the carbon isotopic ratio toward lower values. In this case, we should have measured oxygen isotopic ratios typical for this mass range. Actually, a few M stars in our sample have $^{16}\text{O}/^{18}\text{O} > 1000$ but only one, R Ser, also has $^{12}\text{C}/^{13}\text{C} < 20$. It should be noted that in $^{16}\text{O}/^{18}\text{O}$ measurement of R Ser is based on a single line. In addition, the period of R Ser is not as large as that expected for a massive Mira star.

We note the presence of six stars in our sample with $^{16}\text{O}/^{17}\text{O} < 200$ but only one (RU Her) that shows a large $^{16}\text{O}/^{18}\text{O}$. In this case, however, the HBB hypothesis can be discarded because the predicted HBB carbon isotopic ratio is ~ 5 while the measure value is 25 ± 5 . As discussed by Lebzelter et al. (2015) the most obvious explanation for peculiar values of the oxygen isotopic ratio is that these are fossil records of an anomalous composition, possibly a ^{16}O depleted environment, where these stars were formed. In conclusion, we do not find clear evidence for stars undergoing HBB.

5.4. S and C stars: third dredge-up imprints

Twelve LPVs in our sample have $^{12}\text{C}/^{13}\text{C}$ ratios above 30. In this group, four objects are classified as S stars and three as C stars. Assuming that the abundances are intrinsic these LPVs have experienced TDU events. For six stars of this group observations of Tc in their spectra (Little et al. 1987; Lebzelter & Hron 2003; Uttenthaler et al. 2011) confirm the TDU hypothesis. The mass range of this subset of stars should be $1.5 M_{\odot} < M < 3 M_{\odot}$.

There are two C-stars in our sample that have a $^{12}\text{C}/^{13}\text{C}$ ratio clearly incompatible with the TDU hypothesis, VX And and U Cyg. As discussed in the previous section an intrinsic C star should have $^{12}\text{C}/^{13}\text{C} > 25$ if its initial mass is between $1.5M_{\odot}$ and $2M_{\odot}$ or > 70 if the initial mass is larger than $2 M_{\odot}$. VX And and U Cyg have carbon isotopic ratios clearly smaller than 25, 13 ± 5 and 14 ± 6 , respectively. They are likely J- or R-type C stars with an initial mass $< 1.5 M_{\odot}$. For VX And this conclusion is also supported by its large $^{16}\text{O}/^{17}\text{O}$, 1349 ± 500 , a value that fits expectations for an AGB star with $M \sim 1.3 M_{\odot}$. Indeed Barnbaum et al. (1996) classifies VX And as J4.5 or MS5. U Cyg does not present as clear a case.

U Cyg is classified by Sanford (1950) as R8 and Np. Barnbaum (1994) classifies it as Nep. Keenan (1957) notes the presence of a weak Li 6708 line. U Cyg shows a very low $^{16}\text{O}/^{17}\text{O}$, 158 ± 30 , that is outside the range of any reasonable nucleosynthesis scenario. In principle, such

a low $^{16}\text{O}/^{17}\text{O}$ may be due to deep extra-mixing that occurred during the RGB and/or the AGB. However, in that case $^{12}\text{C}/^{13}\text{C}$ should be ~ 5 and $^{16}\text{O}/^{18}\text{O} > 10^5$ (see Figure 9 and 10).

The $^{12}\text{C}/^{13}\text{C}$ for UX Dra is 28 ± 7 . This is marginally compatible with a TDU scenario. Both the $^{12}\text{C}/^{13}\text{C}$ and the $^{16}\text{O}/^{17}\text{O}$, 631 ± 250 , are compatible with a newborn C-star with a mass of about $1.6 \pm 0.1 M_{\odot}$ and $\text{C}/\text{O} \sim 1$. This scenario is also supported by the s-process overabundances observed by Abia et al. (2001). However, the short period of 168 days and the semi-regular variability type are more appropriate for an early-AGB star.

The other three carbon stars in the sample, S Cep, V Hya, and R Lep, are clearly well above the TDU limit of 25 for $^{12}\text{C}/^{13}\text{C}$. S Cep has long period of 487 days and a large $^{12}\text{C}/^{13}\text{C}$, 224 ± 130 , both compatible with an evolved AGB star with $M \leq 2 M_{\odot}$. Similarly long period, 529 days, and high $^{12}\text{C}/^{13}\text{C}$, 200 ± 50 , are found for V Hya. With these features V Hya is probably an intrinsic C star of $2.5 \pm 0.5 M_{\odot}$ approaching the AGB tip. However, although affected by a large error the $^{16}\text{O}/^{17}\text{O}$, 1122 ± 400 , is probably too high. V Hya is a peculiar LPV with high velocity flows and has been suggested as a nascent proto-PN (Sahai et al. 2009). R Lep has a long period of 432 days coupled to $^{12}\text{C}/^{13}\text{C} = 34 \pm 5$ and $^{16}\text{O}/^{17}\text{O} = 676 \pm 120$ in accord with expectations for an evolved low-mass AGB star of $M \sim 1.6 M_{\odot}$ close to the AGB tip.

Finally RZ Per, the single SC star in our sample, has a low $^{12}\text{C}/^{13}\text{C}$ of 9 ± 3 . SC stars are intriguing objects whose nature has not been unveiled yet (Hedrosa et al. 2013). Due to the complex spectrum the oxygen isotopic ratios could not be derived for this star.

5.5. O-rich presolar grains from AGB stars.

Presolar grains⁴, i.e. dust grains formed in the material ejected by stars of different mass and composition and found in pristine meteorites, bring clear signatures of the nucleosynthesis and mixing processes occurred in the parent stars (Zinner 1998). Among them the majority of the O-rich grains, oxides and silicates, are believed to originate in the wind of AGB stars (Nittler 2009). Therefore, the isotopic abundances measured in these presolar material can be directly compared to the corresponding abundances we measured in O-rich LPVs. In Figure 14 oxygen isotopic ratios in presolar grains (squares) are compared to the values found for the O-rich AGB stars in our sample. The lifetime of O-rich grains in the interstellar medium is ~ 500 Myr (Jones et al. 1996). Thus the parent stars of the presolar grains should have ended their life within a few hundreds Myr before the formation of the solar system. If the stars were low-mass AGBs then the time of their formation coincides with a very early epoch of the Milky Way evolution. On the contrary, the AGB stars in our sample were formed no more than a couple of Gyr ago and, in any case, much later than the birth of the solar system. This occurrence likely implies a difference in the initial

⁴In the meteoritic abundance community the isotopic ratios are the inverse of the astronomical convention. In this section, we adopt their convention to allow comparison with literature data.

chemical composition: the present day generation of AGB stars is, on the average, more metal-rich than the AGB stars from which the presolar grains formed.

Keeping in mind this remark and following Nittler (2009) we note that the majority of the O-rich grains, those belonging to group 1 in Figure 14, should come from low-mass AGB stars with $1.2 < M/M_{\odot} < 2$. As stressed in the previous sections, the O isotopic ratios in these stars are determined by i) the initial composition and ii) the first dredge up. The quoted mass range is, in fact, compatible with the spread of $^{17}\text{O}/^{16}\text{O}$ resulting after the first dredge up. The sub-solar $^{18}\text{O}/^{16}\text{O}$ of group 1 grains also supports such an hypothesis. Indeed, it is compatible with the ^{18}O depletion caused by the first dredge up on material whose original composition was nearly solar. The spread of $^{17}\text{O}/^{16}\text{O}$ observed in the stars of our sample is almost identical to that of the O-rich presolar grains confirming that they are AGB stars with mass similar to those from which the grains originated. However, at variance with the grain abundances the majority of the AGB stars in our sample present super-solar $^{18}\text{O}/^{16}\text{O}$. This occurrence must reflect a difference in the initial composition, namely a ^{16}O depletion and/or a ^{18}O enhancement. This is not surprising considering the different formation epoch. Indeed, chemical evolution models predict a steadily increase with time of the $^{18}\text{O}/^{16}\text{O}$ (Prantzos et al. 1996). A similar conclusion was obtained by Lebzelter et al. (2015) by studying the $^{18}\text{O}/^{16}\text{O}$ ratios of giant stars in young open clusters.

Grains belonging to group 2, those showing rather low $^{18}\text{O}/^{16}\text{O}$, probably originated in stars with masses similar to those of group 1 but they must have suffered an additional ^{18}O depletion likely caused by some extramixing that took place during the AGB phase (Nittler et al. 2008). Note that only one star in our sample, SV Cas, shares O isotopic ratios similar to those of group 2 grains. Perhaps this occurrence indicates that AGB extramixing is rarer in more metal-rich AGB stars.

The few grains belonging to groups 3 and 4 are believed to have a different origin, interstellar medium for group 3 and supernova ejecta for group 4. Note, however, that some Miras of our sample show O isotopic ratios similar to those of group 4 grains.

As noted by Nittler (2009), no presolar grains from massive AGB, $M > 4 M_{\odot}$, have been found so far. Interestingly, we did not found Miras showing the chemical peculiarities caused by the HBB, a feature expected for massive AGB stars.

6. CONCLUSIONS

We have presented $^{12}\text{C}/^{13}\text{C}$, $^{16}\text{O}/^{17}\text{O}$, and $^{16}\text{O}/^{18}\text{O}$ isotopic ratios for a sample of 46 long period AGB Mira and SRa variables. The sample was selected mainly by apparent infrared brightness and represents the population I field near the sun. Measurement of the $^{12}\text{C}/^{13}\text{C}$ and $^{16}\text{O}/^{17}\text{O}$ ratios allow the main sequence mass for these field stars to be categorized. Among the AGB stars we have studied:

- the majority of the M stars have masses $M < 2 M_{\odot}$;
- all three S stars are the result of the occurrence of third dredge-up episodes;
- three of the C stars are compatible with the TDU hypothesis and another C star is likely undergoing TDU;
- two C stars are either J or peculiar N-type resulting from binary mass transfer or merger;
- no clear evidence of HBB has been found in any of our sample stars.

The overall abundance changes are in accord with previous analysis of O-rich presolar grains and reinforce the hypothesis about the low-mass AGB origin of this stardust.

The work of TL has been supported by the Austrian Science Fund FWF under project number P23737-N16. The National Optical Astronomy Observatory is operated by the Association of Universities for Research in Astronomy under cooperative agreement with the National Science Foundation. This research was facilitated by the SIMBAD database, operated by CDS in Strasbourg, France, and NASA’s Astrophysics Data System Abstract Service. We acknowledge with thanks the variable star observations from the AAVSO International Database contributed by observers worldwide and used in this research.

REFERENCES

- Abia, C. & Isern, J. 1997, MNRAS, 289, L11
- Abia, C. & Isern, J. 2000, ApJ, 536, 438
- Abia, C., Busso, M., Gallino, R., et al. 2001, ApJ, 559, 1117
- Abia, C., Domínguez, I., Gallino, R., Busso, M., Straniero, O., de Laverny, P., & Wallerstein, G. 2003, Pub. Astro. Soc. Australia, 20, 314
- Abia, C., Palmerini, S., Busso, M., & Cristallo, S. 2012, A&A, 548, A55
- Barnbaum, C. 1994, ApJS, 90, 317
- Barnbaum, C., Stone, R.P.S., & Keenan, P.C. 1996, ApJS, 105, 419
- Bessell, M.S. 2005, ARAA, 43, 293
- de Bièvre, P., Gallet, M., Holden, N.E., & Barnes, I.L. 1984, J. Phys. Chem. Ref. Data, 13, 809
- Boothroyd, A. I., Sackmann, I.-J., & Wasserburg, G. J. 1995, ApJ, 442, L21

- Boothroyd, A.I. & Sackmann, I.J. 1999, *ApJ*, 510, 232
- Busso, M., Palmerini, s., Maiorca, E., Cristallo, s., Straniero, O., Abia, C., Gallino, R. & La Cognata, M. 2010, *ApJ*, 717, L47
- Cristallo, S., Straniero, O., Piersanti, L., & Gobrecht, D. 2015, *ApJS*, 219, 40
- Charbonnel, C., Brown, J. A., & Wallerstein, G. 1998, *A&A*, 332, 204
- Charbonnel, C., Brown, J. A., & Wallerstein, G. 1999, *STSci Symp. Ser.12: Unsolved Problems in Stellar Evolution*, 5
- Charbonnel, C., & Lagarde, N. 2010, *A&A*, 522, A10
- Dearborn, D.S.P. 1992, *PhR*, 210, 367
- Doherty, C. L., Siess, L., Lattanzio, J. C., & Gil-Pons, P. 2010, *MNRAS*, 401, 1453
- Doherty, C. L., Gil-Pons, P., Lau, H. H. B., Lattanzio, J. C., & Siess, L. 2014, *MNRAS*, 437, 195
- Dominy, J.F. & Wallerstein, G. 1987, *ApJ*, 317, 810
- Dominy, J.F., Hinkle, K.H., Lambert, D.L., Hall, D.N.B., & Ridgway, S.T. 1978, *ApJ*, 223, 949
- El Eid, M.F. 1994, *A&A*, 285, 915
- Feast, M.W. 2009, in: "AGB Stars and Related Phenomena", eds. Ueta, T., Matsunaga, N., Ita, Y., Tokyo, p.48
- Gehrz, R. 1989, in 'Interstellar Dust' Proc. IAU Symp. 135, ed. L. J. Allamandola & A. G. G. M. Tielens. (Kluwer, Dordrecht, p.445
- George, Urban, & LeFloch 1994, *J Mol Spec*, 165, 500
- Gilroy, K.K. 1989, *ApJ*, 347, 835
- Gilroy, K. K., & Brown, J. A. 1991, *ApJ*, 371, 578
- Goorvitch & Chackerian 1994 *ApJS*, 91, 483
- Goorvitch & Chackerian 1994 *ApJS*, 92 311
- Gratton, R. G., Sneden, C., Carretta, E., & Bragaglia, A. 2000, *A&A*, 354, 169
- Hall, D.N.B., Ridgway, S.T., Bell, E.A., & Yarborough, J.M. 1979, *Proc. SPIE*, 172, 121
- Harris, M.J. & Lambert, D.L. 1984, *ApJ*, 285, 674
- Harris, M.J., Lambert, D.L., & Goldman, A. 1987a, *MNRAS*, 224, 237

- Harris, M.J., Lambert, D.L., Hinkle, K.H., Gustafsson, B., & Eriksson, K. 1987b, *ApJ*, 316, 294
- Hedrosa, R.P., Abia, C., Busso, M., et al. 2013, *ApJ*, 768, L11
- Herzberg, G. 1950, “Molecular Spectra and Molecular Structure I. Spectra of Diatomic Molecules,” (Van Nostrand Reinhold, New York), p 124.
- Hinkle, K.H., Lambert, D.L., & Snell, R.L. 1976, *ApJ*, 210, 684
- Hinkle, K.H. 1978, *ApJ*, 220, 210
- Hinkle, K.H. & Barnes, T.G. 1979, *ApJ*, 234, 548
- Hinkle, K.H., Hall, D.N.B., & Ridgway, S.T. 1982, *ApJ*, 252, 697
- Hinkle, K.H., Scharlach, W.W.G., & Hall, D.N.B. 1984, *ApJS*, 56, 1
- Hinkle, K.H., Lebzelter, T., & Scharlach, W.W.G., 1997, *AJ*, 114, 2686
- Hinkle, K.H., Aringer, B., Lebzelter, T., Martin, C.L., & Ridgway, S.T. 2000, *A&A*, 363, 1065
- Hoppe, P. 2010, *AIPC*, 1213, 84
- Iben, I., Jr., & Renzini, A. 1983, *ARA&A*, 21, 271
- Ireland, M.J., Scholz, M., & Wood, P.R. 2008, *MNRAS*, 391, 1994
- Jones, A. P., Tielens, A. G. G. M., & Hollenbach, D. J. 1996, *ApJ*, 469, 740
- Jura, M., Kahane, C., & Omont, A. 1988, *A&A*, 201, 80
- Karakas, A.I., Campbell, S.W., & Stancliffe, R.J. 2010, *ApJ*, 713, 374
- Keenan, P.C. 1957, *PASP*, 69, 5
- Khoury, T., de Koter, A., Decin, L., et al. 2014a, *A&A*, 561, A5
- Khoury, T., de Koter, A., Decin, L., et al. 2014b, *A&A*, 570, A67
- Lambert, D.L., Gustafsson, B., Eriksson, K., & Hinkle, K.H. 1986, *ApJS*, 62, 373
- Lambert, D.L., Smith, V.V., Busso, M., Gallino, R., & Straniero, O., 1995, *ApJ*, 450, 302
- Lebzelter, T., Hinkle, K.H., & Hron, J. 1999, *A&A*, 341, 224
- Lebzelter, T. & Hron, J. 2003, *A&A*, 411, 533
- Lebzelter, T., Lederer, M.T., Cristallo, S., et al. 2008, *A&A*, 486, 511
- Lebzelter, T., Nowotny, W., Hinkle, K.H., Höfner, S., Aringer, B. 2014, *A&A*, 567, A143

- Lebzelter, T., Straniero, O., Hinkle, K.H., Nowotny, W., Aringer, B. 2015, *A&A*, 578, A33
- Lederer, M.T., Lebzelter, T., Cristallo, S., et al. 2009, *A&A*, 509, 913
- Little, S.J., Little-Marenin, I.R. & Hagen-Bauer, W. 1987, *AJ*, 94, 981
- Lodders, K., Palme, H. & Gail, H.P. 2009, *Landolt-Börnstein - Group VI, Volume 4B*, 44
- Lugaro, M., Herwig, F., Lattanzio, J. C., Gallino, R., & Straniero, O. 2003, *ApJ*, 586, 1305
- Maiorca, E., Magrini, L., Busso, M., Randich, S., Palmerini, S., & Trippella, O. 2012, *ApJ*, 747, 53
- McSaveny, J.A., Wood, P.R., Scholz, M., Lattanzio, J.C., & Hinkle, K.H. 2007, *MNRAS*, 378, 1089
- Maior, U. & Tescari, E. 2015, *MNRAS*, 453, 3798
- Milam, S.N., Woolf, N.J., & Ziurys, L.M. 2009, *ApJ*, 690, 837
- Nittler, L.R., Alexander, C.M.O'D., Gallino, R., Hoppe, P., Nguyen, A.N., Stadermann, F.J., & Zinner, E.K. 2008, *ApJ*, 682, 1450
- Nittler, L. R. 2009, *PASA*, 26, 271
- Nordhaus, J., Busso, M., Wasserburg, G. J., Blackman, E. G., & Palmerini, S. 2008, *ApJ*, 684, L29
- Norton, R.H. & Beer, R. 1976, *J.Opt.Soc.Am.*, 66, 259
- Pols, O.R., Tout, C.A., Lattanzio, J.C., & Karakas, A.I. 2001, in "Evolution of Binary and Multiple Star Systems," eds. Ph. Podsiadlowski et al., *ASP Conference Series*, 229, 31
- Prantzos, N., Aubert, O., & Audouze, J. 1996, *A&A*, 309, 760
- Ramstedt, S. & Olofsson, H. 2014, *A&A*, 566, A145
- Ridgway, S.T. & Hinkle, K.H. 1992, *ESOC*, 40, 213
- Sahai, R., Sugerman, B.E.K., & Hinkle, K.H. 2009, *ApJ*, 699, 1015
- Sanford, R. 1950, *ApJ*, 111, 262
- Savage, C., Apponi, A.J., Ziurys, L.M., & Wyckoff, S. 2002, *ApJ*, 578, 211
- Schöier, F.L. & Olofsson, H. 2000, *A&A*, 359, 586
- Sedlmayr, E. 1994, in 'Molecules in the Stellar Environment', *Proc. IAU Colloq. 146*, ed. U. G. Jorgensen, *Lecture Notes in Physics*, 428, 163
- Sengupta, S., Izzard, R.G. & Lau, H.H.B. 2013, *A&A*, 559, A66
- Straniero, O., Gallino, R., & Cristallo, S. 2006, *Nuclear Physics A*, 777, 311

- Straniero, O., Domínguez, I., Cristallo, S., & Gallino, R. 2003, *PASA*, 20, 389
- Straniero, O., Cristallo, S., & Piersanti, L. 2014, *ApJ*, 785, 77
- Tomkin, J., Luck, R.E. & Lambert, D.L. 1976, *ApJ*, 210, 694
- Tsuji, T. 2008, *A&A*, 489, 1271
- Uttenthaler, S., van Stiphout, K., Voet, K., et al. 2011, *A&A*, 531, 88
- Vassiliadis, E. & Wood, P.R. 1993, *ApJ*, 413, 641
- Wallace, L. & Hinkle, K.H. 1997, *ApJS*, 111, 445
- Wallerstein, G., Balick, B., Alcolea, J., Bujarrabal, V., & Vanture, A.D. 2011, *A&A*, 535, A101
- Wasserburg, G.J., Boothroyd, A.I. & Sackmann, I.J. 1995, *ApJ*, 447, L37
- Wood, P.R. 2015, *MNRAS*, 448, 3829
- Wood, P.R. & Zarro, D.M. 1981, *ApJ*, 247, 247
- Wouterloot, J.G.A., Henkel, C., Brand, J., & Davis, G.R. 2008, *A&A*, 487, 237
- Zinner, E. 1998, *Annual Review of Earth and Planetary Sciences*, 26, 147

	1st dup	RGB (AGB) extra-mixing	2nd dup	3rd dup	HBB
$^{12}\text{C}/^{13}\text{C}$	↓	↓	⇩	↑	↓
$^{16}\text{O}/^{17}\text{O}$	↓	⇩	⇩		⇩
$^{16}\text{O}/^{18}\text{O}$	↑	⇩	⇩		↑

Fig. 10.— Influence of the various mixing events on the carbon and oxygen isotopic ratios. Filled arrows indicate a significant variation of the isotopic ratio while open arrows indicate small variations (smaller than the observational errors).

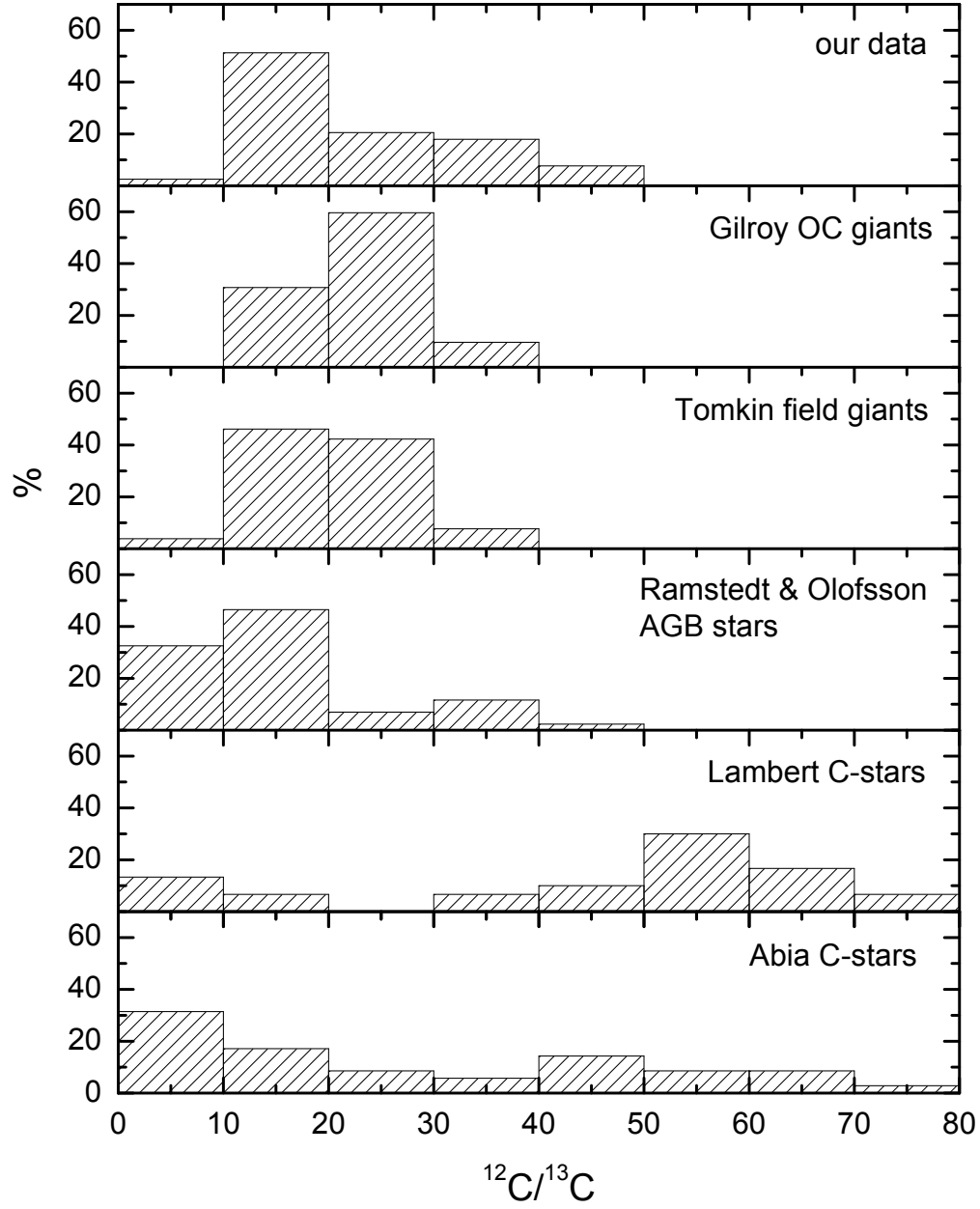


Fig. 11.— Histograms of the $^{12}\text{C}/^{13}\text{C}$ distribution in various samples of evolved stars. From top to bottom: (1) Data presented in this paper. (2) Gilroy (1989). (3) Tomkin et al. (1976). (4) Ramstedt & Olofsson (2014). (5) Lambert et al. (1986). (6) Abia & Isern (2000) and Abia et al. (2001). See text for details.

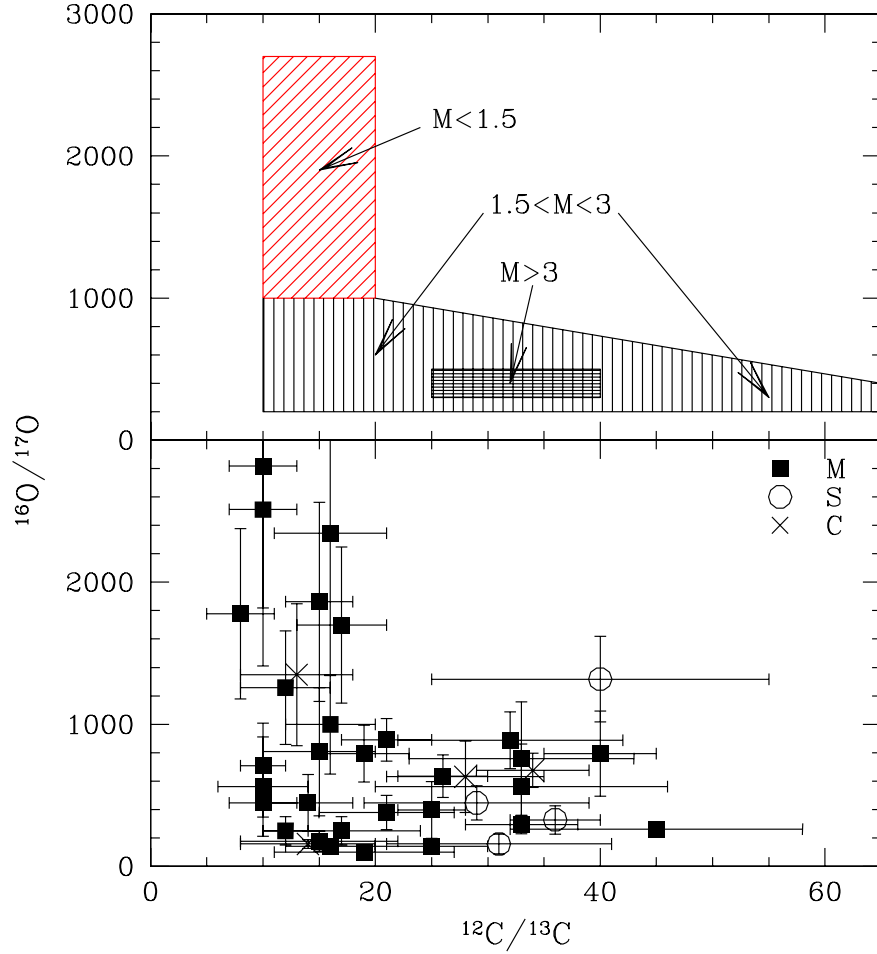


Fig. 12.— $^{16}\text{O}/^{17}\text{O}$ versus $^{12}\text{C}/^{13}\text{C}$ diagram. Upper panel: Shaded areas delimit the parameter space where we expect to find AGB stars with the three labeled mass ranges. The location of AGB stars with $M > 6$ is not shown. For such stars, the occurrence of the HBB should imply quite low values of both $^{16}\text{O}/^{17}\text{O}$ and $^{12}\text{C}/^{13}\text{C}$. Lower panel: Derived values for the sample stars plotted in the parameter space seen in the upper panel. Note the different symbols used for M-type, S-type, and C-type stars.

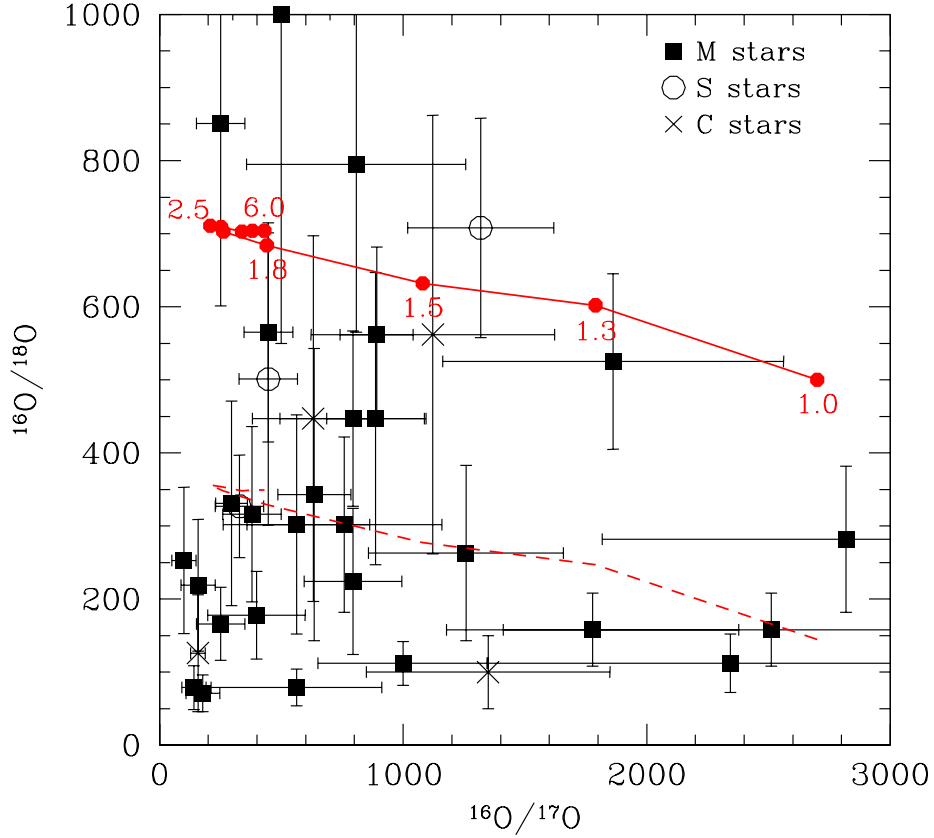


Fig. 13.— Positions of the stars included in our sample in the $^{16}\text{O}/^{18}\text{O}$ versus $^{16}\text{O}/^{17}\text{O}$ diagram. The solid line represents model predictions for solar composition AGB stars of different (indicated) initial mass. The dashed line shows this relation for an initial ^{18}O abundance twice solar. As in Figure 12 different symbols are used to mark the M-, S-, and C-type stars.

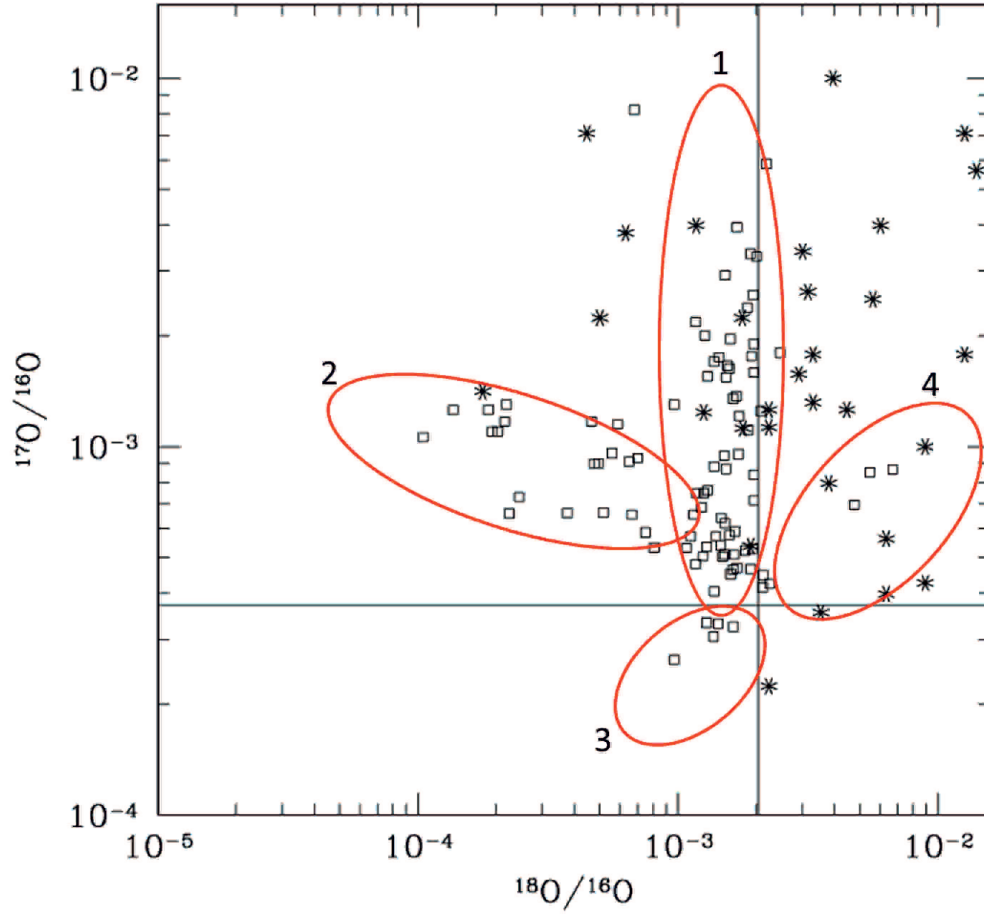


Fig. 14.— Open symbols, abundances measured in O-rich presolar grains from Table 2 of Nittler et al. (2008). Starred symbols, Mira measurements, this paper. The light solid lines show the solar values for the two oxygen isotopes while the ellipses delimit regions occupied by different groups of grains (see text).

Table 1. Observations

Star	Type	Date	Int. Time (min.)	Apodizing Fcn ^a	Resolution (cm ⁻¹)	S/N (peak)
R And	M	78 Oct 17	68	2	0.074	114
VX And	SRa	79 Jul 18	135	2	0.070	69
R Aql	M	77 Aug 26	60	2	0.084	98
R Aqr	M	83 Sep 14	17	2	0.070	160
T Ari	M	83 Jan 22	94	2	0.070	60
T Ari	M	85 Jul 2	52	2	0.070	51
R Aur	M	84 Aug 8	34	2	0.070	80
T Cam	M	83 Jun 4	42	2	0.070	30
TX Cam	M	83 Jun 4	44	2	0.070	109
R Cnc	M	83 Jan 22	43	2	0.070	154
S CMi	M	83 May 24	67	2	0.070	55
S CrB	M	83 Dec 24	70	2	0.070	44
T Cas	M	76 May 13	24	0	0.083	72
T Cas	M	82 Nov 26	51	2	0.070	171
R Cas	M	77 Mar 28	31	0	0.083	56
R Cas	M	84 Jun 12	17	2	0.070	205
R Cas	M	84 Sep 5	17	2	0.070	138
R Cas	M	85 Sep 1	25	2	0.070	72
SV Cas	SRa	83 May 21	68	2	0.070	49
S Cep	M	80 Jan 25	84	2	0.070	93
T Cep	M	77 Nov 8	32	2	0.084	106
o Cet	M	79 Nov 2	17	2	0.070	144
o Cet	M	80 Jan 4	42	2	0.070	210
o Cet	M	80 Feb 27	33	2	0.070	211
o Cet	M	80 Jun 3	17	2	0.070	102
o Cet	M	80 Jun 24	17	2	0.070	122
o Cet	M	80 Oct 30	17	2	0.070	156
o Cet	M	84 Aug 7	17	2	0.070	172
R Cyg	M	84 May 20	85	2	0.070	26
U Cyg	M	76 Aug 18	67	0	0.110	83
RU Cyg	SRa	76 May 15	53	0	0.104	30
RU Cyg	SRa	84 Oct 13	50	2	0.070	106
RZ Cyg	SRa	84 Mar 22	103	2	0.070	57
χ Cyg	M	78 Oct 17	17	2	0.070	280
χ Cyg	M	79 Feb 8	17	2	0.070	260
χ Cyg	M	80 Feb 27	17	2	0.070	150
UX Dra	SRa	80 Feb 27	118	2	0.070	60
RT Eri	M	83 Aug 29	120	2	0.070	99
U Her	M	83 Sep 27	68	2	0.070	93
RU Her	M	84 Feb 21	85	2	0.070	53

Table 1—Continued

Star	Type	Date	Int. Time (min.)	Apodizing Fcn ^a	Resolution (cm ⁻¹)	S/N (peak)
R Hya	M	83 Dec 24	40	2	0.070	82
R Hya	M	84 Apr 21	34	2	0.070	134
V Hya	SRa	79 Nov 27+28	168	2	0.070	153
W Hya	SRa	84 Feb 13	33	2	0.070	202
R Leo	M	82 Nov 26	34	2	0.070	171
R Lep	M	80 Feb 27	126	2	0.070	128
T Lep	M	84 Sep 5	84	2	0.070	93
RS Lib	M	84 Apr 21	51	2	0.070	64
R LMi	M	82 Nov 26	34	2	0.070	55
X Oph	M	78 Oct 17	69	2	0.074	145
X Oph	M	80 Feb 27	34	2	0.070	110
S Ori	M	83 Jan 22	76	2	0.070	138
U Ori	M	76 Dec 6	60	0	0.060	101
U Ori	M	84 Apr 21	68	2	0.070	141
R Peg	M	83 May 20	44	2	0.070	43
W Peg	M	83 May 20	64	2	0.070	85
RZ Peg	M	77 Jun 30	92	2	0.153	49
IR Per	SRa	83 Aug 29	67	2	0.070	97
V384 Per	M	79 Oct 17	135	2	0.074	70
R Ser	M	84 Feb 13	75	2	0.070	99
BG Ser	M	84 Jun 12	69	2	0.070	58
IK Tau	M	83 Dec 23	41	2	0.070	151
R UMi	SRa	83 Sep 13	101	2	0.070	97
S UMi	M	83 Jan 22	42	2	0.070	116
SS Vir	SRa	79 Dec 6	177	2	0.070	56
β And	... ^c	76 Jun 6	39	0	0.084	... ^b
μ Gem	... ^c	76 Sep 29	54	0	0.084	50
α Her	... ^c	77 Feb 19	30	0	0.084	83
α Her	... ^c	77 Jun 24	31	0	0.084	90
β Peg	... ^c	76 May 12	48	0	0.084	76

^aNorton & Beer (1976)

^bNo reverse scan

^cReference spectrum

Note. — The variability class is taken from the GCVS.

Table 2. Isotopic ratios.

Star	Type	Period [d]	Phase	T_{excit} [K]	$^{12}\text{C}/^{13}\text{C}$	$^{16}\text{O}/^{17}\text{O}$	$^{16}\text{O}/^{18}\text{O}$
R And	S-Mira	409	0.59	2500	40±15	1318±300	708±150
VX And	C-SRa	369	0.41:	3200	13±5	1349±500	100±50
R Aqr	Mira	387	0.56:	3100	16±5	2344±1000	112±40 ^a
R Aql	Mira	293	0.69	3100	8:	224:	398: ^a
T Ari	Mira	323	0.4/0.71	2900/3200	15±5	807±450	795±230
R Aur	Mira	458	0.13	2950	33±13	562±300	302±150
T Cam	S-Mira	374	0.52	2600	31±10	158±70	219±90
TX Cam	Mira	557	0.52	2800	21±6	380±120	316±120
S CMi	Mira	332	0.69	2700	18±5	490:	398:
R Cas	Mira	431	0.18	3000	12±4	–	–
T Cas	Mira	445	0.60	2800	33±5	295±65	331±140
SV Cas	SRa	276	0.36:	3000	10±2	708±300	5623±2500 ^a
R Cnc	Mira	361	0.11	3050	17±4	1698±550	–
S Cep	C-Mira	487	0.97	3100	224±130	>1000	>700
T Cep	Mira	388	0.20	2900	33±10	759±400	302±120
o Cet	Mira	332	0.20	3100	10±3	2818±1000	282±100 ^a
S CrB	Mira	360	0.00	3000	–	500±200	1000±450
χ Cyg	S-Mira	407	multiple		36±4	328±100	327±70
R Cyg	S-Mira	426	0.89	2400	29±10	447±120	501±200 ^a
U Cyg	C-Mira	465	0.64	2500	14±6	158±30	126±80
RU Cyg	SRa	234	0.29/0.37	3000/3100	32±10	887±200	447±200
RZ Cyg	SRa	276	0.54	3050	40±5	794±300	447±120 ^a
UX Dra	C-SRa	168:	0.52:	2900	28±7	631±250	447±250 ^a
RT Eri	Mira	371	0.72	3100	15±7	178±70	71±25
U Her	Mira	405	0.48	3200	19±8	100±50	253±100 ^a
RU Her	Mira	485	0.78	3000	25±5	141±50	2239±500 ^a
R Hya	Mira	388	0.42/0.72	3000/2900	26±4	635±150	343±200
V Hya	C-SRa	529	–	3300	200±50	1122±500	562:
W Hya	SRa	382	0.15	3250	16±4	1000±350	112±30
R Leo	Mira	313	0.61	2900	10±3	447±100	565±150
R LMi	Mira	372	0.58	2900	12±2	251±100	851±250 ^a
R Lep	C-Mira	432	0.10	3100	34±5	676±120	–
T Lep	Mira	368	0.04	3200	19±4	794±200	224±100
RS Lib	Mira	218	0.81	3800	16±4	141±50	79±30
X Oph	Mira	334	0.17/0.71	3150/3000	12±4	1258±400	263±120
S Ori	Mira	419	0.43	2900	45±13	263±50	1585±550
U Ori	Mira	372	0.24/0.43	3100/2600	25±10	4467±1000	447±150
R Peg	Mira	378	0.15	3250	10±4	562±350	79±25
W Peg	Mira	344	0.70	3000	17±7	251±100	166±50
RZ Peg	SC-Mira	439	0.63	2400	9±5	–	–
IR Per	SRa	175	–	3050	25±3	398±200	178±60

Table 2—Continued

Star	Type	Period [d]	Phase	T _{excit} [K]	¹² C/ ¹³ C	¹⁶ O/ ¹⁷ O	¹⁶ O/ ¹⁸ O
R Ser	Mira	357	0.62	2950	14±4	447±200	1995±900 ^a
BG Ser	Mira	143	0.42:	2950	21±4	891±150	562±120
IK Tau	Mira	450:	0.44	2800	8±3	1778±600	158±50
R UMi	SRa	324	0.63	3000	15±3	1862±700	525±120
S UMi	Mira	326	0.26	3000	10±3	2511±1100	158±50

^aRatio ¹⁶O/¹⁸O based on a single line.

Note. — See 3.4 for details on the uncertainty given in the Table.

Table 3. Comparison with literature values.

Star	$^{12}\text{C}/^{13}\text{C}$			$^{16}\text{O}/^{17}\text{O}$			$^{16}\text{O}/^{18}\text{O}$		
	Lit. value	Ref.	this paper	Lit. value	Ref.	this paper	Lit. value	Ref.	this paper
R And	24	(2)	40±15						
	33	(7)							
VX And	13±3	(1)	13±5	400±175	(4)	1349±500	>150	(4)	100±50
	6	(13)							
TX Cam	15	(2)	21±6						
R Cas	9	(2)	12±4						
χ Cyg	40	(2)	35±4						
	39	(7)							
R Cyg	24±5	(8)	29±10	860	(8)	447±120			
	26	(2)							
	34	(7)							
UX Dra	32±5	(1)	28±7	1650±450	(4)	631±250	2250±925	(4)	447±250
	25:	(3)							
	3±1	(2)							
	26	(12)							
V Hya	69±15	(1)	200±50	4100±1800	(4)	1122±500	>700	(4)	560:
W Hya	18±10	(5)	16±4	1250±600	(6)	1000±350	190±150	(6)	112±30
	10	(2)							
R Leo	6±2	(2)	10±3						
R Lep	62±15	(1)	34±5						
	22	(2)							
	90:	(3)							
IK Tau	10±4	(2)	8±3						
RZ Peg	12	(11)	9±5						
β And	11±3	(9)	13±3	155±40	(9)	224±70	425±112	(9)	1000±400
μ Gem	13±2	(9)	16±5	325±112	(9)	630±250	475±137	(9)	1120±330
	10.5±1.2	(10)		798±73	(10)				
α Her	17±4	(9)	14±3	180±60	(9)	355±110	550±200	(9)	562±120
	11.1±0.7	(10)		102±8	(10)				
β Peg	7±1	(9)	9±1	1050±375	(9)	>1900	425±112	(9)	1000±250
	7.7±0.5	(10)		>2500	(10)				

References. — (1) Lambert et al. (1986); (2) Ramstedt & Olofsson (2014); (3) Schöier & Olofsson (2000); (4) Harris et al. (1987b); (5) Khouri et al. (2014a); (6) Khouri et al. (2014b); (7) Wallerstein et al. (2011); (8) Dominy & Wallerstein (1987); (9) Harris & Lambert (1984); (10) Tsuji (2008); (11) Hedrosa et al. (2013); (12) Abia et al. (2001); (13) Abia & Isern (2000)

Note. — Where literature values are listed without an uncertainty it was not possible to deduce the uncertainty

from the paper unambiguously. Throughout this paper, the uncertainties given are symmetric (see comment in 3.4). In the case that asymmetric uncertainties are given in the literature mean values are given here. For R Cyg, (8) states an uncertainty of +2000 and –600 so in this case a mean value made no sense.

Table 4. Appendix 1 CO $\Delta v=2$ Best Lines

Wavenumber (vacuum cm^{-1})	Wavelength (air \AA)	Isotope		Transition			Number of spectra	
		C	O	v'	v''	Branch		
4001.726	24982.40	12	16	3	1	P	40	6
4037.166	24763.09	12	17	3	1	P	26	4
4037.753	24759.49	12	18	2	0	P	27	5
4037.975	24758.13	12	16	6	4	P	3	5
4049.647	24686.77	12	16	6	4	R	97	8
4055.447	24651.47	12	16	4	2	P	22	7
4055.641	24650.29	13	16	2	0	P	25	6
4056.826	24643.09	12	16	5	3	P	11	4
4057.233	24640.62	12	16	3	1	P	31	4
4061.257	24616.20	12	16	5	3	P	10	4
4064.595	24595.99	12	16	6	4	R	93	13
4066.772	24582.82	12	16	6	4	R	4	7
4068.253	24573.87	13	16	3	1	P	12	10
4068.851	24570.26	12	16	3	1	P	29	9
4069.353	24567.23	13	16	4	2	R	0	9
4069.915	24563.83	12	16	5	3	P	8	7
4070.879	24558.02	12	16	4	2	P	19	7
4071.072	24556.85	13	16	2	0	P	22	5
4094.487	24416.42	13	16	4	2	R	93	4
4096.744	24402.97	12	16	3	1	P	24	5
4097.090	24400.91	12	16	2	0	P	33	4
4098.962	24389.77	12	16	6	4	R	15	5
4099.925	24384.03	12	16	4	2	P	13	6
4100.244	24382.14	13	16	2	0	P	16	10
4110.712	24320.05	12	16	6	4	R	20	7
4110.996	24318.37	12	16	6	4	R	77	11
4112.039	24312.20	13	16	4	2	R	14	4
4113.531	24303.38	12	16	4	2	P	10	6
4113.977	24300.75	13	16	2	0	P	13	8
4115.311	24292.87	12	16	6	4	R	75	10
4116.042	24288.56	12	16	5	3	R	3	9
4116.886	24283.58	12	16	6	4	R	23	9
4117.067	24282.51	13	16	4	2	R	16	8
4118.798	24272.31	12	16	6	4	R	24	5
4119.430	24268.58	12	16	5	3	R	4	8
4121.824	24254.49	13	16	4	2	R	18	6
4123.341	24245.56	13	16	3	1	R	1	4
4125.705	24231.67	12	16	6	4	R	28	9
4126.788	24225.31	13	16	3	1	R	2	4
4130.106	24205.85	12	16	6	4	R	31	6

Table 4—Continued

Wavenumber (vacuum cm^{-1})	Wavelength (air \AA)	Isotope		Transition				Number of spectra
		C	O	v'	v''	Branch	J''	
4140.256	24146.50	12	16	6	4	R	56	8
4140.461	24145.31	12	16	6	4	R	42	9
4144.618	24121.09	13	16	4	2	R	30	10
4145.494	24116.00	13	16	4	2	R	71	4
4147.524	24104.19	12	16	3	1	P	14	5
4148.305	24099.66	13	16	4	2	R	69	6
4150.002	24089.80	13	16	4	2	R	34	9
4150.816	24085.08	13	16	4	2	R	67	5
4151.172	24083.01	13	16	4	2	R	35	7
4151.521	24080.99	12	16	5	3	R	83	6
4151.724	24079.81	13	16	2	0	P	4	4
4156.565	24051.76	13	16	4	2	R	61	5
4157.394	24046.97	13	16	4	2	R	42	7
4157.610	24045.72	13	16	3	1	R	12	6
4158.533	24040.38	13	16	4	2	R	44	5
4159.952	24032.18	13	16	4	2	R	48	5
4160.105	24031.30	13	16	4	2	R	53	4
4160.127	24031.17	13	16	4	2	R	49	5
4160.325	24030.03	13	16	3	1	R	13	4
4161.440	24023.59	12	16	3	1	P	11	7
4161.690	24022.15	12	16	5	3	R	19	5
4162.973	24014.74	13	16	3	1	R	14	4
4163.143	24013.76	13	16	2	0	P	1	4
4163.929	24009.23	12	16	5	3	R	20	17
4165.312	24001.26	12	16	4	2	R	2	4
4166.793	23992.73	13	16	2	0	R	103	12
4168.066	23985.40	13	16	3	1	R	16	4
4168.188	23984.69	12	16	5	3	R	22	7
4168.380	23983.59	12	16	5	3	R	76	4
4168.806	23981.14	12	16	4	2	R	3	12
4169.197	23978.89	12	16	4	2	R	95	18
4170.055	23973.96	12	16	2	0	P	20	5
4172.888	23957.68	13	16	3	1	R	18	7
4174.380	23949.12	12	16	5	3	R	73	14
4174.740	23947.05	12	16	3	1	P	8	5
4175.202	23944.40	12	16	2	0	P	19	4
4176.898	23934.68	12	18	3	1	R	79	6
4177.438	23931.58	13	16	3	1	R	20	4
4177.805	23929.49	13	16	3	1	R	82	7
4177.974	23928.51	12	16	5	3	R	71	9

Table 4—Continued

Wavenumber (vacuum cm^{-1})	Wavelength (air \AA)	Isotope		Transition				Number of spectra
		C	O	v'	v''	Branch	J''	
4180.283	23915.30	12	16	2	0	P	18	4
4180.777	23912.47	12	16	5	3	R	29	4
4182.762	23901.13	12	16	5	3	R	68	12
4183.263	23898.26	12	16	3	1	P	6	7
4184.215	23892.83	13	16	2	0	R	4	4
4185.059	23888.01	12	16	5	3	R	32	4
4185.719	23884.24	13	16	3	1	R	24	15
4185.967	23882.83	12	18	2	0	R	7	5
4186.337	23880.72	12	16	5	3	R	33	4
4186.827	23877.92	12	16	5	3	R	65	6
4188.022	23871.11	12	16	5	3	R	64	5
4188.283	23869.62	12	16	4	2	R	9	6
4188.667	23867.43	12	16	5	3	R	35	10
4192.009	23848.40	12	16	5	3	R	60	7
4192.424	23846.04	12	16	5	3	R	39	6
4192.808	23843.86	12	16	5	3	R	59	7
4192.899	23843.34	13	16	3	1	R	28	6
4193.174	23841.78	12	16	5	3	R	40	5
4197.557	23816.88	13	16	3	1	R	31	15
4197.855	23815.19	12	18	2	0	R	11	5
4198.141	23813.57	12	18	3	1	R	38	4
4198.297	23812.68	13	16	3	1	R	71	15
4199.478	23805.99	12	16	3	1	P	2	7
4200.661	23799.28	12	18	2	0	R	12	6
4201.041	23797.13	13	16	3	1	R	69	7
4201.349	23795.38	12	18	3	1	R	61	5
4202.550	23788.58	12	16	4	2	R	14	7
4209.036	23751.93	13	16	3	1	R	61	16
4209.343	23750.19	12	16	2	0	P	12	4
4209.703	23748.17	13	16	3	1	R	60	7
4209.879	23747.17	13	16	3	1	R	43	11
4210.246	23745.10	12	16	4	2	R	17	9
4210.445	23743.98	13	16	3	1	R	44	6
4210.908	23741.37	12	16	3	1	R	0	5
4212.665	23731.46	12	16	4	2	R	18	7
4213.359	23727.56	12	16	2	0	R	111	10
4213.486	23726.84	13	16	2	0	R	89	5
4220.692	23686.33	12	18	2	0	R	20	6
4222.231	23677.70	12	17	3	1	R	79	4
4225.165	23661.26	12	16	3	1	R	4	7

Table 4—Continued

Wavenumber (vacuum cm ⁻¹)	Wavelength (air Å)	Isotope		Transition				Number of spectra
		C	O	v'	v''	Branch	J''	
4225.651	23658.53	12	16	4	2	R	24	5
4226.419	23654.24	13	16	2	0	R	19	11
4227.088	23650.49	12	18	2	0	R	23	10
4227.354	23649.01	12	16	2	0	P	8	5
4228.553	23642.30	12	16	3	1	R	5	4
4228.943	23640.12	12	16	3	1	R	94	8
4229.084	23639.33	12	18	2	0	R	24	7
4229.392	23637.61	12	16	4	2	R	26	5
4231.152	23627.78	12	16	4	2	R	27	4
4231.402	23626.38	12	16	4	2	R	72	4
4232.441	23620.58	12	16	3	1	R	93	16
4232.837	23618.37	12	16	4	2	R	28	5
4233.313	23615.72	13	16	2	0	R	81	8
4234.449	23609.38	12	16	4	2	R	29	11
4235.116	23605.66	12	16	3	1	R	7	4
4235.446	23603.82	13	16	2	0	R	80	22
4235.545	23603.27	12	18	2	0	R	76	9
4236.323	23598.94	12	16	4	2	R	69	5
4237.103	23594.59	13	16	2	0	R	24	12
4237.448	23592.67	12	16	4	2	R	31	20
4237.803	23590.70	12	16	4	2	R	68	26
4238.034	23589.41	12	18	2	0	R	29	14
4238.290	23587.98	12	16	3	1	R	8	5
4240.522	23575.57	12	16	4	2	R	66	5
4240.897	23573.48	13	16	2	0	R	26	12
4241.761	23568.68	12	16	4	2	R	65	5
4242.921	23562.24	12	16	4	2	R	64	5
4243.216	23560.60	13	16	2	0	R	76	19
4244.648	23552.65	12	16	4	2	R	37	6
4245.002	23550.69	12	16	4	2	R	62	10
4245.258	23549.27	12	18	2	0	R	34	5
4245.584	23547.46	12	16	4	2	R	38	8
4246.069	23544.77	13	16	2	0	R	29	5
4246.445	23542.69	12	16	4	2	R	39	5
4246.766	23540.90	12	16	4	2	R	60	12
4247.938	23534.41	12	16	4	2	R	41	9
4248.821	23529.52	12	16	4	2	R	57	5
4249.607	23525.17	12	16	4	2	R	44	7
4249.797	23524.12	12	16	4	2	R	55	5
4252.602	23508.60	13	16	2	0	R	70	7

Table 4—Continued

Wavenumber (vacuum cm^{-1})	Wavelength (air \AA)	Isotope		Transition				Number of spectra
		C	O	v'	v''	Branch	J''	
4254.535	23497.92	13	16	2	0	R	35	4
4254.994	23495.38	12	18	2	0	R	45	5
4255.130	23494.64	13	16	2	0	R	68	5
4255.455	23492.84	12	18	2	0	R	46	4
4256.796	23485.44	13	16	2	0	R	37	14
4257.821	23479.78	13	16	2	0	R	38	5
4258.775	23474.52	13	16	2	0	R	39	5
4259.659	23469.65	13	16	2	0	R	40	5
4260.472	23465.18	13	16	2	0	R	41	7
4261.108	23461.67	12	16	3	1	R	16	4
4261.884	23457.40	13	16	2	0	R	43	7
4262.266	23455.30	13	16	2	0	R	60	7
4262.483	23454.10	13	16	2	0	R	44	4
4263.011	23451.20	13	16	2	0	R	45	11
4265.405	23438.04	12	16	3	1	R	82	10
4266.090	23434.27	12	16	3	1	R	18	4
4267.542	23426.30	12	16	2	0	R	1	4
4267.904	23424.31	12	16	3	1	R	81	17
4268.472	23421.19	12	16	3	1	R	19	5
4269.709	23414.41	12	17	2	0	R	20	5
4271.942	23402.17	12	17	2	0	R	21	11
4274.106	23390.33	12	17	2	0	R	22	16
4274.317	23389.17	12	16	2	0	R	97	5
4277.270	23373.02	12	16	3	1	R	23	9
4278.234	23367.75	12	16	2	0	R	4	4
4280.171	23357.18	12	17	2	0	R	25	9
4280.580	23354.95	12	17	2	0	R	77	10
4281.228	23351.41	12	16	3	1	R	25	5
4282.051	23346.92	12	17	2	0	R	26	4
4283.860	23337.06	12	17	2	0	R	27	15
4285.598	23327.60	12	17	2	0	R	28	30
4287.265	23318.53	12	17	2	0	R	29	16
4287.806	23315.59	12	17	2	0	R	73	6
4288.665	23310.92	12	16	2	0	R	93	7
4288.859	23309.86	12	17	2	0	R	30	8
4289.829	23304.59	12	16	3	1	R	30	5
4290.382	23301.59	12	17	2	0	R	31	20
4291.834	23293.71	12	17	2	0	R	32	21
4292.042	23292.58	12	16	2	0	R	92	20
4292.409	23290.58	12	17	2	0	R	70	12

Table 4—Continued

Wavenumber (vacuum cm^{-1})	Wavelength (air \AA)	Isotope		Transition				Number of spectra
		C	O	v'	v''	Branch	J''	
4292.749	23288.74	12	16	3	1	R	32	5
4293.213	23286.22	12	17	2	0	R	33	14
4293.789	23283.10	12	17	2	0	R	69	8
4294.097	23281.43	12	16	3	1	R	33	4
4294.638	23278.50	12	16	2	0	R	9	5
4295.092	23276.04	12	17	2	0	R	68	4
4296.318	23269.40	12	17	2	0	R	67	5
4296.567	23268.05	12	16	3	1	R	35	8
4296.834	23266.60	12	16	3	1	R	65	13
4297.467	23263.17	12	17	2	0	R	66	4
4297.959	23260.51	12	16	3	1	R	64	7
4298.736	23256.31	12	16	3	1	R	37	9
4299.003	23254.86	12	16	3	1	R	63	13
4299.969	23249.64	12	16	3	1	R	62	9
4302.166	23237.76	12	16	3	1	R	41	6
4302.390	23236.55	12	16	3	1	R	59	14
4307.670	23208.07	12	16	2	0	R	87	12
4318.678	23148.92	12	16	2	0	R	83	13
4319.649	23143.71	12	16	2	0	R	18	4
4322.066	23130.77	12	16	2	0	R	19	5
4323.687	23122.10	12	16	2	0	R	81	19
4326.068	23109.37	12	16	2	0	R	80	12
4328.367	23097.10	12	16	2	0	R	79	20
4330.585	23085.27	12	16	2	0	R	78	10
4331.003	23083.04	12	16	2	0	R	23	5
4332.721	23073.89	12	16	2	0	R	77	6
4334.775	23062.95	12	16	2	0	R	76	9
4343.807	23015.00	12	16	2	0	R	30	4
4351.876	22972.33	12	16	2	0	R	36	5
4353.130	22965.71	12	16	2	0	R	64	4
4353.964	22961.31	12	16	2	0	R	38	6
4356.528	22947.80	12	16	2	0	R	41	4
4357.857	22940.80	12	16	2	0	R	43	6
4358.407	22937.90	12	16	2	0	R	44	6
4358.534	22937.23	12	16	2	0	R	57	4
4359.597	22931.64	12	16	2	0	R	47	4

Table 5. Appendix 2 CO $\Delta v=3$ Best Lines

Wavenumber (vacuum cm^{-1})	Wavelength (air \AA)	Isotope		Transition				Number of spectra
		C	O	v'	v''	Branch	J''	
5568.210	17954.19	12	16	10	7	P	41	4
5587.946	17890.78	12	16	9	6	P	48	4
5631.431	17752.63	12	16	11	8	P	20	4
5638.522	17730.30	12	16	8	5	P	51	7
5647.716	17701.44	12	16	11	8	P	17	6
5669.443	17633.60	12	16	12	9	R	7	4
5669.814	17632.45	12	16	7	4	P	56	7
5675.918	17613.49	12	16	12	9	R	53	6
5682.291	17593.73	12	16	9	6	P	36	8
5703.868	17527.18	12	16	5	2	P	68	5
5705.649	17521.70	12	16	8	5	P	43	4
5717.374	17485.77	12	16	9	6	P	31	5
5718.004	17483.84	12	16	6	3	P	59	19
5721.446	17473.33	12	16	8	5	P	41	5
5726.507	17457.88	12	16	4	1	P	73	4
5732.851	17438.57	13	16	10	7	R	18	4
5735.251	17431.27	12	16	10	7	P	15	5
5736.846	17426.42	12	16	8	5	P	39	4
5740.304	17415.92	12	16	10	7	P	14	14
5743.633	17405.83	12	16	9	6	P	27	4
5749.617	17387.71	12	16	7	4	P	47	6
5749.945	17386.72	12	16	9	6	P	26	5
5750.848	17383.99	12	16	10	7	R	76	6
5756.157	17367.96	12	16	9	6	P	25	4
5764.027	17344.25	12	16	10	7	P	9	7
5766.905	17335.59	12	16	11	8	R	16	6
5769.111	17328.96	12	16	11	8	R	46	6
5777.117	17304.95	12	16	11	8	R	24	5
5777.461	17303.91	12	16	11	8	R	39	4
5778.586	17300.55	12	16	11	8	R	26	7
5778.846	17299.77	12	16	11	8	R	37	8
5785.690	17279.30	12	16	9	6	P	20	4
5787.609	17273.58	12	16	8	5	P	32	4
5788.154	17271.95	12	16	9	6	R	84	7
5792.472	17259.07	13	16	9	6	R	10	3
5794.460	17253.15	12	16	8	5	P	31	4
5796.039	17248.45	13	16	6	3	P	36	5
5800.339	17235.67	13	16	8	5	P	9	14
5806.802	17216.48	13	16	9	6	R	49	4
5807.072	17215.68	12	16	10	7	R	1	15

Table 5—Continued

Wavenumber (vacuum cm^{-1})	Wavelength (air \AA)	Isotope		Transition				Number of spectra
		C	O	v'	v''	Branch	J''	
5807.482	17214.47	12	16	9	6	P	16	6
5807.862	17213.34	12	16	8	5	P	29	8
5811.792	17201.70	12	16	4	1	P	65	10
5812.198	17200.50	13	16	9	6	R	21	4
5812.673	17199.09	12	16	9	6	P	15	9
5814.411	17193.95	12	16	8	5	P	28	10
5823.326	17167.63	12	16	5	2	P	56	8
5825.198	17162.11	12	16	10	7	R	7	11
5827.631	17154.95	12	16	9	6	P	12	7
5827.848	17154.31	12	16	10	7	R	8	9
5828.946	17151.08	12	16	7	4	P	37	6
5829.743	17148.73	13	16	6	3	P	31	13
5829.961	17148.09	12	16	10	7	R	55	8
5831.489	17143.60	12	16	9	6	R	76	5
5831.747	17142.84	13	16	7	4	P	18	13
5837.386	17126.28	12	16	10	7	R	12	10
5838.576	17122.79	12	16	8	5	R	89	8
5843.621	17108.01	12	16	7	4	P	35	4
5845.644	17102.09	12	16	8	5	P	23	8
5849.957	17089.48	12	16	10	7	R	19	5
5850.808	17086.99	12	16	7	4	P	34	6
5851.016	17086.38	12	16	5	2	P	53	6
5855.015	17074.71	13	16	6	3	P	27	4
5860.051	17060.04	12	16	5	2	P	52	6
5861.097	17057.00	13	16	6	3	P	26	5
5861.983	17054.41	12	16	4	1	P	60	7
5864.580	17046.86	13	16	7	4	R	79	5
5864.883	17045.98	12	16	7	4	P	32	12
5865.172	17045.14	13	16	8	5	R	9	4
5866.077	17042.51	13	16	7	4	P	11	14
5867.339	17038.85	12	16	9	6	R	68	12
5869.569	17032.37	13	16	4	1	P	46	7
5870.761	17028.92	12	16	9	6	P	2	10
5871.298	17027.36	12	16	9	6	R	67	5
5872.366	17024.26	12	16	7	4	R	96	8
5874.335	17018.55	12	16	8	5	P	18	6
5875.578	17014.95	12	16	6	3	P	41	17
5875.907	17014.00	13	16	8	5	R	53	13
5876.304	17012.85	13	16	8	5	R	14	10
5877.193	17010.28	13	16	5	2	P	35	6

Table 5—Continued

Wavenumber (vacuum cm ⁻¹)	Wavelength (air Å)	Isotope		Transition				Number of spectra
		C	O	v'	v''	Branch	J''	
5880.057	17001.99	13	16	8	5	R	16	8
5880.785	16999.89	12	16	8	5	R	82	13
5881.385	16998.15	12	16	4	1	P	58	10
5885.568	16986.07	13	16	3	0	P	53	5
5885.983	16984.88	12	16	9	6	R	63	17
5886.206	16984.23	13	16	8	5	R	47	7
5886.570	16983.18	12	16	5	2	P	49	5
5887.172	16981.44	13	16	7	4	R	74	4
5887.680	16979.98	13	16	8	5	R	21	4
5888.411	16977.87	12	16	9	6	R	2	12
5889.367	16975.12	12	16	9	6	R	62	4
5890.324	16972.36	12	16	8	5	P	15	6
5897.101	16952.85	12	16	8	5	R	79	5
5897.737	16951.03	12	16	9	6	R	5	7
5898.311	16949.38	12	16	7	4	P	27	9
5899.424	16946.18	13	16	7	4	R	71	10
5899.510	16945.93	13	16	7	4	P	3	7
5902.305	16937.91	12	16	8	5	R	78	4
5903.426	16934.69	12	16	9	6	R	7	4
5903.760	16933.73	12	16	5	2	P	47	15
5904.100	16932.76	13	16	5	2	P	31	15
5904.694	16931.05	12	16	7	4	P	26	4
5906.263	16926.56	12	16	6	3	P	37	4
5907.271	16923.67	12	16	9	6	R	56	10
5908.253	16920.86	13	16	4	1	P	41	11
5908.690	16919.60	12	16	9	6	R	9	8
5909.192	16918.17	12	16	3	0	P	63	14
5910.202	16915.28	12	16	8	5	P	11	8
5910.976	16913.06	12	16	7	4	P	25	4
5911.163	16912.53	12	16	9	6	R	10	4
5914.913	16901.80	12	16	8	5	P	10	6
5919.521	16888.65	12	16	8	5	P	9	9
5921.924	16881.79	12	16	9	6	R	15	5
5923.755	16876.57	12	16	9	6	R	16	7
5924.026	16875.80	12	16	8	5	P	8	12
5929.213	16861.04	12	16	7	4	P	22	4
5929.499	16860.23	12	16	9	6	R	45	5
5930.003	16858.79	12	16	9	6	R	20	10
5930.845	16856.40	12	16	9	6	R	44	4
5931.500	16854.54	13	16	6	3	P	13	4

Table 5—Continued

Wavenumber (vacuum cm^{-1})	Wavelength (air \AA)	Isotope		Transition				Number of spectra
		C	O	v'	v''	Branch	J''	
5932.080	16852.89	12	16	9	6	R	43	13
5933.203	16849.70	12	16	9	6	R	42	8
5933.554	16848.70	12	16	9	6	R	23	5
5934.215	16846.83	12	16	9	6	R	41	6
5934.521	16845.96	12	16	9	6	R	24	8
5935.905	16842.03	12	16	9	6	R	39	5
5938.842	16833.70	12	16	7	4	R	86	11
5939.122	16832.91	12	16	3	0	P	60	5
5939.729	16831.19	12	16	8	5	R	70	10
5940.472	16829.08	13	16	7	4	R	9	4
5941.321	16826.68	13	16	7	4	R	58	7
5941.639	16825.78	13	16	5	2	P	25	6
5941.961	16824.86	12	16	5	2	R	108	6
5942.376	16823.69	12	16	6	3	P	32	9
5943.884	16819.42	12	16	8	5	R	69	4
5945.013	16816.23	12	16	5	2	P	42	6
5945.445	16815.01	13	16	6	3	P	10	5
5946.534	16811.93	12	16	7	4	P	19	7
5947.923	16808.00	12	16	8	5	R	68	7
5948.868	16805.33	12	16	8	5	P	2	8
5948.906	16805.22	12	16	3	0	P	59	5
5949.298	16804.12	12	16	6	3	P	31	14
5952.642	16794.67	12	16	8	5	P	1	10
5952.968	16793.76	12	16	5	2	P	41	4
5954.258	16790.12	13	16	6	3	P	8	9
5954.585	16789.19	13	16	7	4	R	52	10
5955.111	16787.71	12	16	4	1	P	50	14
5956.119	16784.87	12	16	6	3	P	30	4
5956.464	16783.90	12	16	7	4	R	83	6
5957.570	16780.78	12	16	7	4	P	17	7
5959.002	16776.75	13	16	7	4	R	18	7
5959.130	16776.39	13	16	5	2	P	22	6
5959.348	16775.78	12	16	8	5	R	65	8
5959.634	16774.97	13	16	3	0	P	44	4
5959.877	16774.29	12	16	8	5	R	0	8
5960.823	16771.63	12	16	5	2	P	40	9
5961.320	16770.23	13	16	7	4	R	48	5
5961.580	16769.50	12	16	6	3	R	95	10
5963.337	16764.55	12	16	8	5	R	1	7
5966.390	16755.98	12	16	8	5	R	63	9

Table 5—Continued

Wavenumber (vacuum cm^{-1})	Wavelength (air \AA)	Isotope		Transition				Number of spectra
		C	O	v'	v''	Branch	J''	
5966.692	16755.13	12	16	8	5	R	2	9
5969.942	16746.01	12	16	8	5	R	3	9
5970.566	16744.26	13	16	7	4	R	29	9
5972.567	16738.65	12	16	4	1	P	48	9
5973.356	16736.44	12	16	7	4	P	14	9
5975.081	16731.60	13	16	3	0	P	42	4
5980.789	16715.64	13	16	6	3	R	70	5
5982.398	16711.14	12	16	6	3	P	26	7
5985.177	16703.38	13	16	4	1	P	30	4
5986.377	16700.03	13	16	5	2	P	17	10
5987.431	16697.09	12	16	8	5	R	56	9
5988.216	16694.91	12	16	7	4	P	11	4
5988.715	16693.51	12	16	6	3	P	25	6
5990.158	16689.49	13	16	3	0	P	40	4
5991.251	16686.45	12	16	5	2	P	36	16
5992.124	16684.02	12	16	8	5	R	11	4
5992.418	16683.20	12	16	8	5	R	54	7
5992.962	16681.68	12	16	7	4	P	10	5
5994.418	16677.63	12	16	8	5	R	12	4
5996.374	16672.19	12	16	3	0	P	54	4
5996.605	16671.55	12	16	8	5	R	13	6
5996.953	16670.58	12	16	8	5	R	52	8
6004.668	16649.16	12	16	8	5	R	48	7
6006.581	16643.86	12	16	7	4	P	7	9
6007.058	16642.54	12	16	6	3	P	22	13
6007.851	16640.34	12	16	8	5	R	46	5
6008.263	16639.20	12	16	6	3	R	88	15
6008.911	16637.41	12	16	8	5	R	20	13
6010.238	16633.73	12	16	8	5	R	21	4
6011.456	16630.36	12	16	8	5	R	22	6
6011.786	16629.45	12	16	8	5	R	43	9
6012.025	16628.79	12	16	7	4	R	72	10
6012.567	16627.29	12	16	8	5	R	23	6
6013.569	16624.52	12	16	8	5	R	24	8
6013.852	16623.74	12	16	8	5	R	41	10
6018.466	16610.99	13	16	6	3	R	10	4
6018.777	16610.13	12	16	6	3	P	20	7
6019.264	16608.79	12	16	7	4	P	4	15
6020.082	16606.53	12	16	5	2	P	32	7
6023.283	16597.71	12	16	7	4	P	3	5

Table 5—Continued

Wavenumber (vacuum cm ⁻¹)	Wavelength (air Å)	Isotope		Transition				Number of spectra
		C	O	v'	v''	Branch	J''	
6023.688	16596.59	12	16	3	0	P	51	15
6025.341	16592.04	13	16	6	3	R	13	5
6025.431	16591.79	13	16	6	3	R	55	4
6027.039	16587.36	12	16	5	2	P	31	5
6030.089	16578.97	12	16	6	3	P	18	13
6030.566	16577.66	12	16	4	1	P	41	17
6031.007	16576.45	12	16	7	4	P	1	8
6032.321	16572.84	12	16	6	3	R	84	9
6033.896	16568.51	12	16	5	2	P	30	4
6034.419	16567.08	13	16	4	1	R	91	4
6034.798	16566.04	13	16	6	3	R	18	11
6035.000	16565.48	13	16	6	3	R	50	12
6035.591	16563.86	12	16	6	3	P	17	17
6038.456	16556.00	12	16	4	1	P	40	5
6039.265	16553.78	13	16	6	3	R	21	8
6039.481	16553.19	13	16	6	3	R	47	7
6041.410	16547.91	12	16	3	0	P	49	14
6047.022	16532.55	12	16	7	4	R	63	5
6047.308	16531.77	12	16	5	2	P	28	5
6048.481	16528.56	12	16	7	4	R	3	15
6051.483	16520.36	12	16	6	3	P	14	5
6056.098	16507.77	13	16	4	1	P	18	4
6057.700	16503.41	12	16	7	4	R	6	11
6058.489	16501.26	13	16	5	2	R	70	6
6058.740	16500.58	12	16	3	0	P	47	6
6060.316	16496.28	12	16	5	2	P	26	11
6060.561	16495.62	12	16	7	4	R	7	7
6062.445	16490.49	12	16	7	4	R	58	10
6063.316	16488.12	12	16	7	4	R	8	7
6066.668	16479.01	12	16	5	2	P	25	4
6067.816	16475.89	12	16	7	4	R	56	11
6069.881	16470.29	12	16	6	3	R	77	4
6070.332	16469.07	12	16	7	4	R	55	11
6071.683	16465.40	13	16	4	1	P	15	7
6072.919	16462.05	12	16	5	2	P	24	4
6073.271	16461.09	12	16	7	4	R	12	11
6074.254	16458.43	12	16	4	1	R	102	5
6075.908	16453.95	12	16	6	3	P	9	4
6076.417	16452.57	12	16	4	1	P	35	8
6076.686	16451.84	13	16	4	1	P	14	8

Table 5—Continued

Wavenumber (vacuum cm^{-1})	Wavelength (air \AA)	Isotope		Transition				Number of spectra
		C	O	v'	v''	Branch	J''	
6077.609	16449.35	12	16	7	4	R	14	6
6079.068	16445.40	12	16	5	2	P	23	8
6080.482	16441.57	12	16	6	3	P	8	14
6081.211	16439.60	12	16	7	4	R	50	14
6083.048	16434.64	12	16	7	4	R	49	5
6083.310	16433.93	12	16	7	4	R	17	11
6083.711	16432.85	12	16	4	1	P	34	4
6083.998	16432.07	12	16	3	0	P	44	13
6084.221	16431.47	12	16	6	3	R	74	11
6088.043	16421.15	12	16	7	4	R	20	5
6090.242	16415.23	12	16	5	2	R	88	4
6097.996	16394.35	12	16	4	1	P	32	4
6098.949	16391.79	13	16	5	2	R	12	8
6100.343	16388.04	12	16	3	0	P	42	7
6101.173	16385.81	13	16	5	2	R	13	9
6104.989	16375.57	12	16	4	1	P	31	11
6106.711	16370.95	13	16	5	2	R	53	21
6108.592	16365.91	13	16	5	2	R	52	4
6110.368	16361.16	13	16	5	2	R	51	5
6110.793	16360.02	13	16	5	2	R	18	7
6111.881	16357.11	12	16	4	1	P	30	6
6113.233	16353.49	13	16	4	1	P	6	7
6114.150	16351.04	12	16	5	2	R	84	6
6114.720	16349.51	13	16	3	0	P	21	5
6115.065	16348.59	13	16	5	2	R	48	4
6116.293	16345.31	12	16	3	0	P	40	13
6116.677	16344.28	13	16	5	2	R	22	4
6116.965	16343.51	12	16	6	3	R	0	19
6117.353	16342.47	12	16	6	3	R	66	5
6118.672	16338.95	12	16	4	1	P	29	5
6120.495	16334.09	12	16	6	3	R	1	12
6125.363	16321.11	12	16	4	1	P	28	4
6125.846	16319.82	13	16	3	0	P	19	13
6127.875	16314.41	12	16	6	3	R	63	16
6129.822	16309.23	12	16	5	2	P	14	11
6130.452	16307.56	12	16	6	3	R	4	12
6130.841	16306.52	12	16	5	2	R	81	14
6134.949	16295.60	12	16	5	2	P	13	13
6136.170	16292.36	12	16	5	2	R	80	5
6138.441	16286.33	12	16	4	1	P	26	7

Table 5—Continued

Wavenumber (vacuum cm^{-1})	Wavelength (air \AA)	Isotope		Transition				Number of spectra
		C	O	v'	v''	Branch	J''	
6139.972	16282.27	12	16	5	2	P	12	9
6140.300	16281.40	12	16	6	3	R	59	8
6142.248	16276.24	12	16	6	3	R	8	8
6143.121	16273.92	12	16	6	3	R	58	4
6145.828	16266.76	12	16	6	3	R	57	7
6147.002	16263.65	12	16	3	0	P	36	10
6147.509	16262.31	12	16	6	3	R	10	4
6150.902	16253.34	12	16	6	3	R	55	5
6153.269	16247.09	12	16	6	3	R	54	4
6156.313	16239.05	12	16	5	2	R	76	10
6156.750	16237.90	12	16	6	3	R	14	10
6157.299	16236.45	12	16	4	1	P	23	5
6158.792	16232.51	12	16	6	3	R	15	5
6159.032	16231.88	12	16	5	2	P	8	4
6160.728	16227.42	12	16	6	3	R	16	8
6161.056	16226.55	12	16	5	2	R	75	4
6162.556	16222.60	12	16	6	3	R	17	9
6166.676	16211.76	12	16	6	3	R	47	18
6167.393	16209.88	12	16	6	3	R	20	6
6170.077	16202.83	12	16	6	3	R	22	5
6170.737	16201.09	12	16	6	3	R	44	5
6171.867	16198.13	12	16	6	3	R	43	5
6172.886	16195.45	12	16	6	3	R	42	4
6173.291	16194.39	12	16	6	3	R	25	12
6173.794	16193.07	12	16	6	3	R	41	5
6175.525	16188.53	12	16	6	3	R	28	6
6175.849	16187.68	12	16	6	3	R	38	6
6180.174	16176.36	13	16	3	0	P	8	4
6180.521	16175.45	12	16	5	2	P	3	18
6181.020	16174.14	12	16	4	1	P	19	8
6181.414	16173.11	13	16	4	1	R	15	14
6182.089	16171.34	13	16	4	1	R	54	17
6183.142	16168.59	12	16	3	0	P	31	5
6185.891	16161.41	13	16	4	1	R	52	11
6186.069	16160.94	13	16	3	0	R	77	4
6186.695	16159.31	12	16	4	1	P	18	9
6193.555	16141.41	13	16	4	1	R	47	4
6194.248	16139.60	13	16	4	1	R	23	7
6201.835	16119.86	12	16	4	1	R	83	11
6202.115	16119.13	12	16	5	2	R	65	4

Table 5—Continued

Wavenumber (vacuum cm^{-1})	Wavelength (air \AA)	Isotope		Transition				Number of spectra
		C	O	v'	v''	Branch	J''	
6202.855	16117.21	12	16	5	2	R	2	7
6205.586	16110.11	12	16	5	2	R	64	7
6206.209	16108.50	12	16	5	2	R	3	4
6206.897	16106.71	13	16	3	0	R	72	5
6210.246	16098.02	12	16	3	0	P	27	9
6212.185	16093.00	12	16	5	2	R	62	9
6212.600	16091.92	12	16	5	2	R	5	5
6215.313	16084.90	12	16	5	2	R	61	12
6215.637	16084.06	12	16	5	2	R	6	17
6216.770	16081.13	12	16	3	0	P	26	11
6218.327	16077.10	12	16	5	2	R	60	7
6223.545	16063.62	12	16	4	1	P	11	9
6229.229	16048.97	12	16	5	2	R	11	7
6234.612	16035.11	13	16	3	0	R	64	8
6235.294	16033.36	13	16	3	0	R	6	12
6235.733	16032.23	12	16	3	0	P	23	8
6240.152	16020.87	12	16	5	2	R	16	4
6243.769	16011.59	12	16	5	2	R	18	5
6248.387	15999.76	12	16	5	2	R	21	5
6248.611	15999.19	12	16	5	2	R	46	5
6249.710	15996.37	12	16	5	2	R	22	5
6249.929	15995.81	12	16	5	2	R	45	4
6250.925	15993.26	12	16	5	2	R	23	4
6252.031	15990.43	12	16	5	2	R	24	6
6253.028	15987.88	12	16	5	2	R	25	5
6253.216	15987.40	12	16	5	2	R	42	6
6257.617	15976.16	13	16	3	0	R	55	4
6257.694	15975.96	13	16	3	0	R	15	5
6260.433	15968.97	12	16	4	1	R	71	13
6263.473	15961.22	12	16	4	1	P	2	17
6265.304	15956.56	12	16	3	0	P	18	6
6267.388	15951.25	12	16	4	1	P	1	15
6272.712	15937.71	12	16	3	0	R	85	9
6278.503	15923.01	12	16	4	1	R	1	8
6281.820	15914.61	12	16	3	0	P	15	9
6287.120	15901.19	12	16	3	0	P	14	4
6297.410	15875.21	12	16	3	0	P	12	9
6297.886	15874.01	12	16	4	1	R	7	5
6299.498	15869.94	12	16	4	1	R	60	17
6303.499	15859.87	12	16	4	1	R	9	5

Table 5—Continued

Wavenumber (vacuum cm^{-1})	Wavelength (air \AA)	Isotope		Transition				Number of spectra
		C	O	v'	v''	Branch	J''	
6305.113	15855.81	12	16	4	1	R	58	8
6306.146	15853.21	12	16	4	1	R	10	4
6307.288	15850.35	12	16	3	0	P	10	12
6307.749	15849.19	12	16	4	1	R	57	8
6311.120	15840.72	12	16	4	1	R	12	5
6312.071	15838.33	12	16	3	0	P	9	11
6314.978	15831.04	12	16	4	1	R	54	4
6317.779	15824.03	12	16	4	1	R	15	6
6319.231	15820.39	12	16	4	1	R	52	5
6325.153	15805.58	12	16	4	1	R	19	9
6325.799	15803.96	12	16	3	0	P	6	9
6326.386	15802.50	12	16	4	1	R	48	7
6328.193	15797.98	12	16	4	1	R	21	4
6329.289	15795.25	12	16	4	1	R	46	6
6329.551	15794.59	12	16	4	1	R	22	11
6330.167	15793.06	12	16	3	0	P	5	14
6330.573	15792.04	12	16	4	1	R	45	5
6331.942	15788.63	12	16	4	1	R	24	4
6346.594	15752.18	12	16	3	0	P	1	4
6350.269	15743.06	12	16	3	0	R	69	5
6371.299	15691.10	12	16	3	0	R	5	8
6371.704	15690.10	12	16	3	0	R	63	11
6377.407	15676.07	12	16	3	0	R	7	11
6377.931	15674.78	12	16	3	0	R	61	9
6380.874	15667.55	12	16	3	0	R	60	10
6388.347	15649.23	12	16	3	0	R	11	6
6390.815	15643.18	12	16	3	0	R	12	4
6396.141	15630.16	12	16	3	0	R	54	9
6400.324	15619.94	12	16	3	0	R	52	5
6402.246	15615.25	12	16	3	0	R	51	5
6403.376	15612.50	12	16	3	0	R	18	7
6405.093	15608.31	12	16	3	0	R	19	8
6409.595	15597.35	12	16	3	0	R	22	4
6410.171	15595.95	12	16	3	0	R	46	7
6412.055	15591.36	12	16	3	0	R	24	4
6414.081	15586.44	12	16	3	0	R	26	6
6414.496	15585.43	12	16	3	0	R	42	6
6414.930	15584.38	12	16	3	0	R	27	4
6415.298	15583.48	12	16	3	0	R	41	8
6415.670	15582.58	12	16	3	0	R	28	6

Table 5—Continued

Wavenumber (vacuum cm^{-1})	Wavelength (air \AA)	Isotope		Transition			Number of spectra
		C	O	v'	v''	Branch J''	